Physics – Uspekhi **61** (5) 480 – 510 (2018)

60th ANNIVERSARY OF THE BUDKER INSTITUTE OF NUCLEAR PHYSICS (BINP), SB RAS

PACS numbers: 07.05.Fb, 11.55.Fv, 12.20.Ds, 13.40.Em, 13.66.Bc, 14.60.Ef

Anomalous magnetic moment of the muon

I B Logashenko, S I Eidelman

DOI: https://doi.org/10.3367/UFNe.2018.02.038312

Contents

Abstract. The anomalous magnetic moment of the muon, a_μ, is a unique quantity that allows high-precision tests of the Standard Model. Currently, a difference of 3 to 4 standard deviations is observed between the prediction of the Standard Model and the most precise measurement performed. We present a review of the Standard Model calculations of a_μ. The principles and history of a_μ experiments are presented, and the recent measurement at the Brookhaven National Laboratory, USA, is described in detail. Prospects for further improving the accuracy of both calculations and measurements of a_μ are discussed.

Keywords: anomalous magnetic moment, Standard Model, electron – positron annihilation, vacuum polarization

I B Logashenko Budker Institute of Nuclear Physics, Siberian Branch of the Russian Academy of Sciences, prosp. Akademika Lavrent'eva 11, 630090 Novosibirsk, Russian Federation;
Novosibirsk State University, ul. Pirogova 2, 630090 Novosibirsk, Russian Federation
E-mail: i.b.logashenko@inp.nsk.su
S I Eidelman Budker Institute of Nuclear Physics, Siberian Branch of the Russian Academy of Sciences, prosp. Akademika Lavrent'eva 11, 630090 Novosibirsk, Russian Federation;
Novosibirsk State University, ul. Pirogova 2, 630090 Novosibirsk, Russian Federation;
Lebedev Physical Institute, Russian Academy of Sciences, Leninskii prosp. 53, 119991 Moscow, Russian Federation
E-mail: s.i.eidelman@inp.nsk.su

Received 15 January 2018
Uspekhi Fizicheskikh Nauk **188** (5) 540 – 573 (2018)
DOI: https://doi.org/10.3367/UFNr.2018.02.038312
Translated by K A Postnov; edited by A M Semikhatov

Dedicated to our friend and teacher, Boris Isaakovich Khazin

1. Introduction

The study of magnetic moments of elementary particles started in 1921 with the famous Stern–Gerlach experiment [1]. This and subsequent experiments showed that the magnetic moment of silver atoms takes exactly two values consistent with the Bohr magneton $\pm e\hbar/2m_e$. Only after several years, when Uhlenbeck and Goudsmit assumed the existence of the electron spin [2] and the magnetic moment of silver atoms was recognized to be due to the spin of one valent electron [3], it became clear that the Stern–Gerlach experiment was the first measurement of the electron spin. It is interesting to note that to explain the ferromagnetic effect A Compton assumed as early as 1921 that the electron has a spin and an internal magnetic moment [4].

The magnetic moment $\boldsymbol{\mu}$ of an elementary particle with mass m is related to its spin $\mathbf{s}$ as

$$\boldsymbol{\mu} = g\left(\frac{q\hbar}{2m}\right)\mathbf{s}\,, \tag{1}$$

where g is the gyromagnetic ratio and q is the particle charge. Measurements suggested that $g_e = 2$ for the electron, which was twice as high as expected from the classical limit for orbital momentum. The relativistic Dirac equation [5] proposed in 1928 explained both the electron spin and the value of the gyromagnetic ratio.

World War II hastened the development of microwave techniques. The use of the new techniques in physical laboratories allowed an improvement in measurements by several orders of magnitude. In 1947, a series of precise measurements of the superfine structure of atomic transitions [6, 7] showed that the splitting of levels is somewhat higher than the predicted value, thus likely suggesting that g_e is slightly different from 2. Conventionally, the gyromagnetic

ratio is written in the form

$$g = 2(1 + a)\,, \tag{2}$$

where the coefficient a is referred to as the anomalous magnetic moment. In particular, measurements [7] suggested that $a_e = (1.15 \pm 0.04) \times 10^{-3}$.

In [8, 9], Schwinger was the first to show that the difference of g_e from 2 is due to radiative corrections and calculated the anomalous magnetic moment of the electron in the leading order of the perturbation theory: $a_e = \alpha/(2\pi) \approx 1.16 \times 10^{-3}$, which was in remarkable agreement with experimental measurements. This result, as well as the calculation of the Lamb shift discovered in 1947 [10], was a triumph of the new theory, quantum electrodynamics (QED).

The measurement in [7] was the first in a series of experiments to measure a_e with ever increasing accuracy. In two decades, by the early 1970s, the measurement precision of a_e increased by 3–4 orders of magnitude, up to a few parts per million (ppm). A detailed review of the history of the development of the main methods and results of measurements of the electron gyromagnetic ratio can be found in [11]. Later on, the best results were obtained by the resonance method, which measures one electron or positron captured in a Penning trap [12]. In the best experiments to date [13, 14], the respective measurement uncertainty of a_e and g_e equal to 0.24 parts per billion (ppb) and 0.28 parts per trillion (ppt) has been achieved.

The possibility of measuring the muon anomalous magnetic moment was predicted by Li and Yang as a consequence of their hypothesis of parity violation in weak interactions [15]. Because of the parity violation, muons turn out to be unique laboratory objects: it is relatively easy to produce beams of polarized muons, because muons created from pion decays are longitudinally polarized, and the muon spin direction can then be deduced from the angular distribution of the decay electrons. In other words, nature endowed muons with a 'cost free' polarizer and polarimeter.

The first measurement of the muon gyromagnetic ratio g_μ was carried out at the cyclotron of Nevis Laboratories in the USA in 1957 [16]. The measurement accuracy at that time, $g_\mu = 2.00 \pm 0.10$, did not allow arriving at a conclusion about the muon anomalous moment. However, this experiment established that the muon is a point-like particle (for a composite particle, g_μ can significantly differ from 2) and confirmed the parity violation in pion and muon decays. In 1960, more accurate measurements at the Nevis cyclotron were reported [17]: $g_\mu = 2(1.00122 \pm 0.00008)$, which confirmed to an approximately 10% uncertainty that $a_\mu \approx \alpha/(2\pi)$, where α is the fine structure constant, i.e., that the muon is a heavy analogue of the electron.

The nonzero value of a is a result of the interaction of a particle with virtual particles — fluctuations of quantum vacuum fields. Therefore, measurements of the anomalous magnetic moment allow estimating the total contribution due to all existing fields (interactions), including those that are not described by the Standard Model. The electron anomalous magnetic moment is almost entirely due to electromagnetic interactions. Therefore, high-precision measurements of a_e can be used to test QED, presently through the fifth order of the perturbation theory ($\sim (\alpha/\pi)^5$), and also to improve QED parameters, for example, in order to obtain the most accurate value of the fine structure constant α [13].

The electromagnetic interactions are somewhat less dominant in the case of the muon anomalous magnetic moment. As was first noted in [18], the large mass of the muon increases the contribution due to massive fields relative to the contribution to a_e by a factor $\sim (m_\mu/m_e)^2 \approx 43{,}000$. In other words, the muon enables us to 'look into' the domain of higher q^2 and to 'see' the manifestation of fields beyond QED (strong and weak interactions, and possibly interactions beyond the Standard Model). Therefore, from the very beginning, there has been great interest in measuring a_μ as a more sensitive tool to probe the theory.

The modern physical particle theory, the Standard Model [19–21], was generally completed by the late 1960s. According to the Standard Model, the physics of subatomic world is described by electromagnetic (QED), strong (quantum chromodynamics, QCD), and weak interactions. Thus far, the Standard Model (SM) has demonstrated a remarkable ability to describe phenomena observed in the realm of elementary particles. The newest discoveries, for example, neutrino oscillations, have called for a modification of the SM. However, these modifications turned out to be minor compared to the initial SM formulation, and they perfectly fit into the main theoretical scheme.

Nevertheless, some observations, first of all astrophysical, suggest that the Standard Model is incomplete at the fundamental level. For example, SM offers no possible candidates for dark matter particles or for dark energy, which are reliably deduced from a bulk of astrophysical observations.

There are many theories extending the Standard Model, for example, a family of supersymmetric theories. There are also theories that radically change our view on fundamental physics, such as string theories. However, the existing experimental data presently do not allow deciding in favor of some of these theories. Therefore, one of the main study areas in high-energy physics is the laboratory search for phenomena 'beyond the Standard Model'. Their discovery would hasten the creation of a new, more complete theory of elementary particles and the determination of possible candidates for such a theory.

Experiments at ever increasing particle energies remain the major research area. Special hope is laid on the continuing experiments at the Large Hadron Collider (LHC) enabling the creation of particles with masses up to a few TeV. Another research avenue is performing experiments at relatively small energies but with a very high precision. The purpose of such experiments is to search either for very rare phenomena prohibited or strongly suppressed in the Standard Model or for differences between the measured values of some quantities from the theoretical predictions. Measurements of the muon anomalous magnetic moment represent the most striking example of the latter experiments.

In the 1960–1970s, a series of measurements of the muon anomalous magnetic moment with ever increasing precision was carried out at CERN. The first experiment (CERN I) [22, 23] was able to achieve a relative uncertainty of 0.4% and to confirm the QED prediction for a_μ with contributions of the order of α/π and $(\alpha/\pi)^2$. In the late 1960s, in the second experiment (CERN II) [24], a relative uncertainty of 0.027% was achieved, which enabled testing the QED predictions up to the order of $(\alpha/\pi)^3$. In addition, in this experiment, the muon anomalous magnetic moment was measured for both μ^+ and μ^-. In the 1970s, another series of experiments was performed (CERN III) [25, 26], which for the first time used a method that became a 'gold standard' for subsequent

measurements. The achieved uncertainty of 7.3 ppm (or 0.00073%) makes it possible to 'probe' not only the QED contribution but also the one due to strong interactions with an accuracy of $\sim 10\%$.

The next, and presently the most precise, experiment, measuring the muon anomalous moment, E821 was carried out in the late 1990s–early 2000s at Brookhaven National Laboratory (BNL) [27] in the USA. Generally, the scheme of the experiment was the same as in CERN III. However, numerous improvements of virtually all subsystems and the use of new approaches in the experimental setup enabled the E821 experiment to reach an accuracy 14 times as high as in the CERN III experiment. The analysis of all accumulated statistics allowed measuring the muon anomalous magnetic moment independently for μ^- and μ^+ with an uncertainty of 0.7 ppm. The obtained results are in agreement with and confirm the CPT invariance. The combination of results for μ^- and μ^+ led to a final uncertainty of 0.52 ppm. At this precision level, contributions due to all interactions of the Standard Model become significant.

Of interest is not the value of the muon anomalous magnetic moment itself, but its difference from the calculated value. In the SM, the calculation uncertainty of the electromagnetic (better than 0.001 ppm [28]) and electroweak (better than 0.01 ppm [29, 30]) contributions significantly exceeds the measurement accuracy of a_μ. In the case of strong interactions, the situation is fundamentally different. Their contribution is rather high, ~ 60 ppm, and the present calculation uncertainty is estimated as $\sim 40 \times 10^{-11}$, which is very close to the measurement accuracy for a_μ and is much worse than the calculation accuracy for other contributions. The reason is that the strong interaction contribution a_μ^{had} cannot be calculated from first principles in the perturbation theory due to the nonperturbative nature of QCD. In fact, the only method that presently enables the calculation of the leading contribution to a_μ^{had} is the integration of the total cross section of e^+e^- annihilation into hadrons. The contribution due to each energy interval enters the integral with the weight $\sim 1/E^2$, where E is the energy of the electron and positron in the center-of-mass frame; therefore, the main contribution comes from the low-energy region. Below, we use the kinetic parameter $s = 4E^2$ for the energy scale.

The total cross section of e^+e^- annihilation into hadrons or the closely related cross section ratio $R(s) = \sigma(e^+e^- \to \text{hadrons})/\sigma(e^+e^- \to \mu^+\mu^-)$ is well predicted in QCD for high energies when perturbative methods can be used. However, at low energies, the experimental measurement of $R(s)$ is the only way to determine it. In all existing calculations of a_μ^{had} (e.g., [31, 32]), the integration in the low-energy domain is performed using experimental data, and at high energies using the perturbative QCD predictions. The energy at which the transition from experimental data to calculations occurs varies from 1.8 to 5 GeV in different calculations. Thus, the measurement accuracy of $R(s)$ at low energies (from the threshold value $2m_\pi$ to about 2 GeV in the center-of-mass frame) directly determines the accuracy of calculations of the strong interaction contribution to the muon anomalous magnetic moment and hence the uncertainty of the comparison of the measured and calculated values of a_μ. Here, the systematic measurement error is decisive, because it is not averaged during the integration.

In the energy domain $\sqrt{s} \leqslant 2$ GeV under discussion, it is very difficult to inclusively measure $R(s)$, i.e., to measure the cross section of $e^+e^- \to X$ directly, where X represents any hadron state. This is due to the smallness of the particle number mean multiplicity at these energies, and therefore a highly effective detection requires the knowledge of the process dynamics (in other words, the energy and angular distribution of the secondary particles). However, exactly at these energies, QCD is unable to predict the corresponding distribution. Therefore, to measure $R(s)$, we use the exclusive approach: the cross section $\sigma_X(s)$ is measured separately for each possible final state X, and $R(s)$ is calculated as the sum of all exclusive cross sections. Thus, each possible final state independently contributes to a_μ^{had}, and all these contributions are added. Of all the final states, the simplest hadron channel $e^+e^- \to \pi^+\pi^-$ makes the leading contribution (about 80%).

The most accurate direct measurements of the exclusive cross sections of hadron production were carried out at the Budker Institute of Nuclear Physics, SB RAS, in a series of experiments with CMD-2 (cryogenic magnetic detector, CMD) [33] and SND (spherical neutral detector, SND) [34] at the accelerator–storage complex VEPP-2M (colliding electron–positron beams). The data were taken from 1993 until 2000, with the main results published in the early 2000s. VEPP-2M completed operations in 2001, and a new e^+e^- collider, VEPP-2000, was constructed [35] with a wider working energy range up to 2 GeV and an order-of-magnitude higher luminosity. Two detectors, CMD-3 [36] and modified SND [37], started collecting experimental statistics in 2010. The measurement of $e^+e^- \to$ hadrons cross sections is one of the principal goals of the experiments. The results for some final states have already been published [38].

In the early 2000s, the appearance of new high-luminosity e^+e^- colliders, including B-factories BaBar [39] and Belle [40] and φ-factory KLOE (K_L^0 Long Experiment) [41, 42], made it possible to develop a new method for hadron cross section measurements — the initial-state radiation (ISR) method. The most detailed measurements of cross sections by the ISR method were performed in the BaBar experiment [43].

With all the existing measurements of $R(s)$ taken into account, the calculation uncertainty of a_μ in the Standard Model reached 0.3–0.4 ppm [44, 45]. In the E821 experiment, a difference at a level of 3.5–4 standard deviations is observed between measurements of the muon anomalous magnetic moment and its Standard Model prediction. Considering the complexity of the experiment and calculations, it is premature to interpret such a discrepancy as a reliable manifestation of interactions beyond the Standard Model. Nevertheless, this result has aroused great interest in the scientific community, and it is currently the most significant deviation between the SM predictions and laboratory experiments.

In this review, we discuss state-of-the-art of measurements of the muon anomalous magnetic moment and its calculation in the Standard Model.

2. Muon anomalous magnetic moment in the Standard Model

In the Standard Model, all interactions except gravitational ones (electromagnetic, strong, and weak) provide significant contributions to the muon anomalous magnetic moment:

$$a_\mu = a_\mu^{\text{QED}} + a_\mu^{\text{had}} + a_\mu^{\text{EW}} . \tag{3}$$

2.1 Contribution due to electromagnetic interactions

The contribution $a_\mu^{\rm QED}$ due to electromagnetic interactions dominates, the next important contribution due to strong interactions being smaller by a factor of 10^{-4}. To date, calculations through the fifth order in the perturbation theory have been carried out. Although the calculation uncertainty of the QED contribution significantly exceeds the measurement errors, it is of interest to discuss this contribution and factors determining the uncertainty in more detail. In addition, it is of interest to compare the results of calculations of $a_\mu^{\rm QED}$ and $a_{\rm e}^{\rm QED}$: in these calculations, an identical set of Feynman diagrams is used, but the results are significantly different because different types of diagrams dominate.

The electromagnetic contribution is traditionally written as the expansion [46]

$$a_\mu^{\rm QED} = A_1 + A_2\left(\frac{m_\mu}{m_{\rm e}}\right) + A_2\left(\frac{m_\mu}{m_\tau}\right) + A_3\left(\frac{m_\mu}{m_{\rm e}}\,,\,\frac{m_\mu}{m_\tau}\right), \quad (4)$$

where A_1 is the contribution universal for all leptons. In the diagram representation, it corresponds to diagrams that either have no lepton loops or contain only loops of the same leptons that are present in the external legs (i.e., muons in the case of $a_\mu^{\rm QED}$ and electrons in the case of $a_{\rm e}^{\rm QED}$). Other contributions correspond to diagrams with loops in which leptons differ from those in the external legs. Clearly, the contributions A_2 and A_3 arise only in the respective second and third orders of the perturbation theory.

Each of the contributions A_i can be represented in the form of an expansion in α:

$$A_i = A_i^{(2)}\left(\frac{\alpha}{\pi}\right) + A_i^{(4)}\left(\frac{\alpha}{\pi}\right)^2 + A_i^{(6)}\left(\frac{\alpha}{\pi}\right)^3 + A_i^{(8)}\left(\frac{\alpha}{\pi}\right)^4 + A_i^{(10)}\left(\frac{\alpha}{\pi}\right)^5 + \dots . \quad (5)$$

It is also convenient to represent the final result as an expansion in α:

$$a_\mu^{\rm QED} = C_1\left(\frac{\alpha}{\pi}\right) + C_2\left(\frac{\alpha}{\pi}\right)^2 + C_3\left(\frac{\alpha}{\pi}\right)^3 + C_4\left(\frac{\alpha}{\pi}\right)^4 + C_5\left(\frac{\alpha}{\pi}\right)^5 + \dots , \quad (6)$$

where the coefficients C_i are the sums of the corresponding contributions $A_1^{(2i)}$, $A_2^{(2i)}$, and $A_3^{(2i)}$.

In the leading order of the perturbation theory (Fig. 1), only the universal contribution exists:

$$C_1 = A_1^{(2)} = \frac{1}{2}\,. \quad (7)$$

This result was first obtained by Schwinger [9] in 1948.

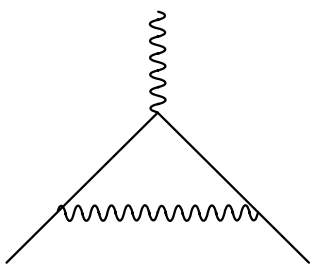

Figure 1. Leading-order $[\alpha/(2\pi)]$ contribution to the magnetic moment.

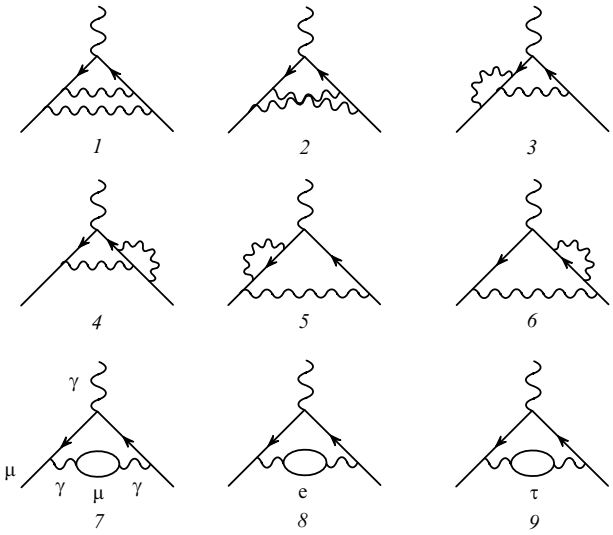

Figure 2. Next-to-leading order contributions to a_μ [45].

In the next-to-leading order of the perturbation theory, the QED contribution is described by 9 diagrams (Fig. 2). Diagrams *1–7* are universal; the corresponding contribution A_1 was obtained in 1957 [47, 48]. The approximate expression for the electron vacuum polarization (diagram *8* in Fig. 2) was obtained in 1957 [49, 50], and the exact one only 10 years later, in 1966 [51]. Much later, a compact form for this expression was found [52]. Ultimately, in the second order of the perturbation theory we have (see, e.g., [53])

$$\begin{aligned} A_1^{(4)} &= -0.32847896557919378\dots , \\ A_2^{(4)}\left(\frac{m_\mu}{m_{\rm e}}\right) &= 1.0942583111(84)\,, \\ A_2^{(4)}\left(\frac{m_\mu}{m_\tau}\right) &= 0.000078064(25)\,, \\ C_2 &= 0.765857410(27)\,. \end{aligned} \quad (8)$$

We note that errors are given for $A_2^{(4)}$, while both $A_1^{(4)}$ and $A_1^{(2)}$ are calculated exactly. This is because $A_2^{(4)}$ depends on the external parameters $m_\mu/m_{\rm e}$ and m_μ/m_τ, which are only known up to some uncertainty.

By comparing these results with similar calculations of $a_{\rm e}$ in the second order of the perturbation theory [53],

$$\begin{aligned} A_1^{({\rm e},4)} &= -0.32847896557919378\dots , \\ A_2^{({\rm e},4)}\left(\frac{m_{\rm e}}{m_\mu}\right) &= 5.19738670(28)\times 10^{-7}\,, \\ A_2^{({\rm e},4)}\left(\frac{m_{\rm e}}{m_\tau}\right) &= 1.83762\,(60)\times 10^{-9}\,, \\ C_2^{\rm e} &= -0.32847844400290(60)\,, \end{aligned} \quad (9)$$

it is possible to note that if $C_1^\mu = C_1^{\rm e}$ in the leading order, then C_2^μ and $C_2^{\rm e}$ differ significantly in the next-to-leading order, and the calculation uncertainty of $C_2^{\rm e}$ is significantly higher because contributions depending on the lepton mass are suppressed. These results clearly illustrate peculiarities of the lepton vacuum polarization on different scales. When the mass of a lepton in the loop is much smaller than that of a lepton in external legs (electron loops in the calculation of a_μ),

the one-loop contribution is proportional to a large value of the logarithm $\ln(m_\mu/m_e) \approx 5.3$, i.e., is significantly enhanced. In the opposite case, where the mass of a lepton in the loop is much larger than that of a lepton in the external legs (τ-lepton loops in the calculation of a_μ), the single loop is proportional to $(m_\mu/m_\tau)^2 \approx 0.0036$, i.e., is significantly suppressed.

In the third order, the electromagnetic contribution is described by more than 100 diagrams. The universal contribution is described by 72 diagrams. Numerical calculations of these diagrams were completed by the beginning of the 1990s [54]. Analytic calculations took more than 30 years, and the final result was obtained in 1996 [55].

Contributions depending on the lepton mass ratios are described by diagrams in which one of the leptons in internal loops is substituted by an electron or a τ lepton. These contributions can be divided into two groups: polarization ones, in which a lepton loop is inserted in one of the photon lines, and light-by-light (LbL) scattering lines (Fig. 3). Analytic expressions for the first and second groups were obtained in [56] and [57]. The LbL scattering contributions with an electron loop that first appeared in the third order dominate because they contain terms $\sim \pi^2 \ln(m_\mu/m_e)$: the sum of polarization contributions with electron loops is $A_2^{(\mathrm{pol},6)}(m_\mu/m_e) = 1.920455130(33)$, and the total LbL scattering contribution is $A_2^{(\mathrm{LbL},6)}(m_\mu/m_e) = 20.94792489(16)$.

In the third order, contributions of type A_3 appear, in which both electron and τ lepton loops are present. The analytic expression for the A_3 contribution was obtained in 1999 [58] and later independently confirmed in [59].

The combination of all third-order contributions of the perturbation theory gives [53]

$$\begin{aligned} A_1^{(6)} &= 1.181241456587\ldots, \\ A_2^{(6)}\left(\frac{m_\mu}{m_e}\right) &= 22.86838002\,(20), \\ A_2^{(6)}\left(\frac{m_\mu}{m_\tau}\right) &= 0.00036051(21), \\ A_3^{(6)}\left(\frac{m_\mu}{m_e}, \frac{m_\mu}{m_\tau}\right) &= 0.00052766(17), \\ C_3 &= 24.05050964(43). \end{aligned} \tag{10}$$

In the fourth order , the total number of diagrams exceeds 1000. The large number and complexity have not allowed their analytic calculation. Starting from the fourth order, the calculational tool is numerical integration, which was developed and perfected over many years by Kinoshita et al. [54].

The universal contribution in the fourth order is described by 891 diagrams. The numerical integration of these diagrams was completed by 1990 [60–64] and was later improved in [65–69]. In 2017, the result of a semianalytic calculation of the universal contribution that took about 20 years was published [71]. In this approach, the calculation of 891 diagrams was reduced to a calculation of 334 master integrals, which were computed with an extremely high precision (9600 significant digits). By assuming that the values of these integrals can be expressed through some irrational numbers ($\ln 2$, the Riemann zeta function $\zeta(n)$, harmonic polylogarithms, etc.), the authors used the PSQL algorithm [72] to search for integer-valued relations and found rational coefficients before the corresponding terms. The result of this semianalytic calculation

$$\begin{aligned} A_1^{(8)} = &-1.912245764926445574152647 1674 \\ &39830054060873390658725345\ldots \end{aligned} \tag{11}$$

is in perfect agreement with the numerical integration results given below.

As in the preceding orders of the perturbation theory, the leading contribution to C_4 comes from diagrams with electron loops, i.e., $A_2^{(8)}(m_\mu/m_e)$. In total, there are 469 such diagrams. This contribution was first found numerically in [46]. Later, errors were found in the initial calculations related to the insufficient accuracy of the 8-byte real arithmetic (double precision in the Fortran code) and to insufficient statistics of Monte Carlo simulations. Development of the calculation methods and improvement of the numerical code enable a significant increase in the accuracy and reliability of the results [28, 73]. Some of the diagrams were calculated analytically [70, 74–77]. The minor contribution of diagrams with τ-lepton loops was calculated numerically.

The combination of all fourth-order contributions gives [28]

$$\begin{aligned} A_1^{(8)} &= -1.91298(84), \\ A_2^{(8)}\left(\frac{m_\mu}{m_e}\right) &= 132.6852(60), \\ A_2^{(8)}\left(\frac{m_\mu}{m_\tau}\right) &= 0.04234(12), \\ A_3^{(8)}\left(\frac{m_\mu}{m_e}, \frac{m_\mu}{m_\tau}\right) &= 0.06272(4), \\ C_4 &= 130.8734(60). \end{aligned} \tag{12}$$

The uncertainty of calculations is determined by the statistical accuracy of the numerical integration by the Monte Carlo method.

In the fifth order of the perturbation theory, the number of diagrams is several dozen thousand. The universal contribution itself is determined by 12,627 diagrams, and until recently, only an estimate of this contribution was available. In 2012, the first results of numerical calculations of all diagrams determining the universal contribution were presented in [68] and later improved in [69]. The initial

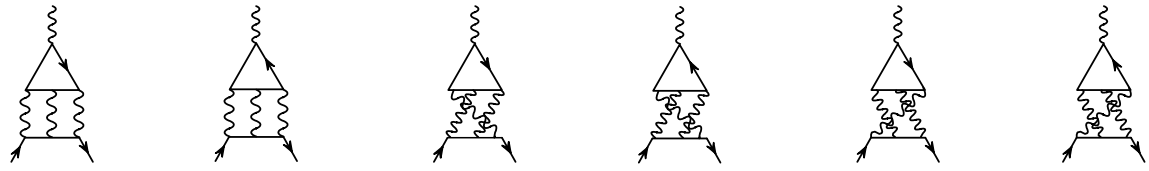

Figure 3. Third-order electromagnetic contributions to a_μ due to light-by-light scattering.

estimate of the leading contribution with electron loops, $A_2^{(10)}(m_\mu/m_e)$, was performed in 1990 [46]. Independent, more precise estimates were obtained in [78–81]. The full fifth-order contribution was calculated only in 2012 [28]. Ultimately, in the fifth order of the perturbation theory, one finds [26, 68]

$$\begin{aligned} A_1^{(10)} &= 7.795(336)\,, \\ A_2^{(10)}\left(\frac{m_\mu}{m_e}\right) &= 742.18(87)\,, \\ A_2^{(10)}\left(\frac{m_\mu}{m_\tau}\right) &= -0.068(5)\,, \\ A_3^{(10)}\left(\frac{m_\mu}{m_e}\,,\frac{m_\mu}{m_\tau}\right) &= 2.011(10)\,, \\ C_5 &= 751.917(932)\,. \end{aligned} \tag{13}$$

As in the fourth order, the calculation uncertainty is determined by the statistical error of the numerical Monte Carlo integration.

The sixth-order contribution is currently unknown; however, initial estimates [28, 82] show that it can exceed the uncertainty of the fifth-order contribution.

To calculate $a_\mu^{\rm QED}$ using expansion (6), in addition to the coefficients C_i discussed above, the expansion parameter α/π must be known. Interestingly, the most precise value of the fine structure constant α is inferred in [69] from measurements of the electron anomalous magnetic moment a_e [14] by assuming that the contribution due to interactions beyond the Standard Model can be ignored:

$$\frac{1}{\alpha} = 137.0359991570(29)(27)(18)(331)\,. \tag{14}$$

Of the four contributions presented above to determine the accuracy of α, the first three correspond to the calculation errors (of the fourth and fifth order and the uncertainty of the weak and strong interaction contributions), and the last, the leading one, corresponds to the measurement error of a_e.

Table 1 lists the expansion coefficients C_i and the contributions of the corresponding orders $C_i(\alpha/\pi)^i$ to $a_\mu^{\rm QED}$ according to [45]. For comparison, similar expansion coefficients C_i^e for $a_e^{\rm QED}$ are given. The values of the coefficients are slightly different from those given above, because they are recalculated taking more precise values of α, m_μ/m_e, and m_τ/m_e into account [83]. A principal difference between a_e and a_μ can be seen: in the first case, the expansion coefficients remain small and change sign, while in the second case the coefficients rapidly increase with the expansion order. As mentioned above, this is related to the domination of different diagrams: the universal contribution for a_e and diagrams with electron loops for a_μ. Despite the rapid increase in the coefficients, the expansion parameter α/π is sufficiently small to provide good conversion of the series. It is also interesting that the leading order mostly contributes to the calculation uncertainty in $a_\mu^{\rm QED}$: although the expansion coefficient C_1 is known exactly, it is so large that the determination uncertainty of α becomes significant.

Table 1. Contributions to $a_\mu^{\rm QED}$ of various orders of the perturbation theory.

Order	C_i^e	C_i^μ	$C_i^\mu(\alpha/\pi)^i$, $\times 10^{11}$
1	0.5	0.5	116,140,973.2420(260)
2	− 0.32847844400	0.765857423(16)	413,217.6270(90)
3	1.181234017	24.05050982(28)	30,141.9022(4)
4	− 1.9113(18)	130.8734(60)	380.9900(170)
5	9.16(58)	751.92(93)	5.0845(63)

The final electromagnetic contribution to the muon anomalous magnetic moment is [45]

$$\begin{aligned} a_\mu^{\rm QED} = \big[&116584718.859 \pm 0.026 \pm 0.009 \pm 0.017 \\ &\pm 0.006(\pm 0.034)\big] \times 10^{-11}\,, \end{aligned} \tag{15}$$

where the first four errors respectively correspond to the uncertainties in α, the lepton mass ratio, and fourth- and fifth-order calculations. The combined final uncertainty in $a_\mu^{\rm QED}$ is estimated to be 0.034×10^{-11}, or 0.29 ppb, which is several orders of magnitude better than the measurement error of a_μ.

2.2 Contribution due to weak interactions

The contribution due to electroweak interactions in the leading order of the perturbation theory was independently calculated by several groups [84–87] in 1992, almost immediately after the proof [88, 89] of the renormalizability of the then-recently formulated Standard Model [19, 20]. This contribution is determined by the two diagrams shown in Fig. 4, which partially cancel each other:

$$\begin{aligned} a_\mu^{(2)\,\rm EW} &= \frac{\sqrt{2}G_F m_\mu^2}{16\pi^2}\left(\frac{10}{3}\,(\rm W) - \frac{5-(1-4\sin^2\Theta_W)^2}{3}\,(\rm Z)\right) \\ &= \big(388.71(0)\,(\rm W) - 193.90(1)\,(\rm Z)\big) \times 10^{-11} \\ &= 194.81(1) \times 10^{-11}\,, \end{aligned} \tag{16}$$

where G_F is the Fermi constant and Θ_W is the Weinberg angle.

The contribution due to the diagram with the Higgs boson exchange is negligibly small due to the smallness of the corresponding coupling constant.

In the early 1990s, the weak interaction contribution was rather 'exotic': it was two orders of magnitude smaller than the measurement error of a_μ. Only with the beginning of the planning of the experiment at BNL was interest aroused in a more precise calculation of the weak interaction contribution. The first estimate of the leading second-order contributions [90] published in 1992 was unexpected: the second-order contribution proved to be very significant, about 20% of the leading-order contribution,

$$a_\mu^{(4)\,\rm EW} \approx (-42 \pm 5) \times 10^{-11}\,, \tag{17}$$

due to the logarithmic enhancement $\sim \ln(M_Z/m_f)$ of individual diagrams. This can be compared to the expected level of electromagnetic corrections to the leading-order contribu-

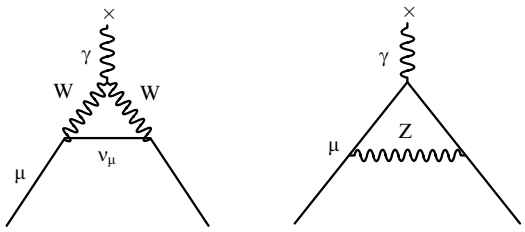

Figure 4. Leading-order contributions to a_μ due to weak interactions.

tion:

$$a_\mu^{(4)\,\mathrm{EW},\gamma} \sim \frac{\sqrt{2}G_\mathrm{F}m_\mu^2}{16\pi^2}\frac{\alpha}{\pi} \approx 0.27\times 10^{-11}\,. \tag{18}$$

The full calculation of the weak interaction contribution to the next-to-leading order of the perturbation theory turned out to be a difficult problem: this contribution is described by 1678 diagrams. Especially difficult is the need to take loop diagrams with light quarks into account. In the second order, triangle diagrams appear, an example of which is shown in Fig. 5. A subset of such diagrams with lepton loops was taken into account in [90]. However, it is known that the Adler–Bell–Jackiw axial anomaly [91–93] arises in such diagrams, which cancels if diagrams with all fermions of one flavor are summed. Therefore, accounting for triangle diagrams with quark loops that partially compensate lepton loops is required. The first estimation of the contribution due to triangle diagrams with fermion loops was obtained in [94], and the full calculation of this contribution was carried out in [95]. The contribution of other diagrams without fermion loops was first calculated in [29], which enabled calculating the full second-order contribution due to weak interactions. This result was later improved in [96, 97]. The weak interaction contribution depends on the Higgs boson mass m_H. After the Higgs boson discovery and the determination of the mass [98, 99], the currently final second-order contribution is [30]

$$a_\mu^{(4)\,\mathrm{EW}} = (-41.20 \pm 0.22 \pm 0.72)\times 10^{-11}\,, \tag{19}$$

where the first contribution to the error is due to the uncertainty in the Higgs boson mass m_H and the top quark mass m_t, and the second contribution is due to the calculation uncertainty of hadron loops. Surprisingly, after multi-year efforts and significant improvement in the calculation methods, the final result proved to be very close to the initial estimate (17) [90].

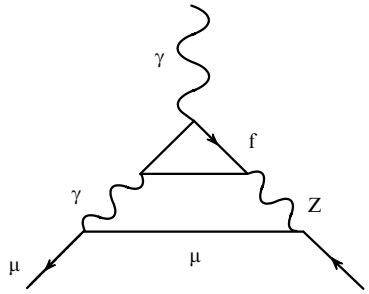

Figure 5. Example of triangle diagrams occurring in the next-to-leading order in calculations of the weak interaction contributions.

An estimate of the weak interaction contribution in the third order was obtained in [96, 97] in the logarithmic approximation:

$$a_\mu^{(6)\,\mathrm{EW}} \approx (0.16 \pm 0.20)\times 10^{-11}\,. \tag{20}$$

Finally, the weak interaction contribution to the muon anomalous magnetic moment is [30]

$$a_\mu^{\mathrm{EW}} = (153.6 \pm 1.0)\times 10^{-11}\,, \tag{21}$$

where the error comes from the uncertainty in m_H and m_t, as well as the calculation uncertainty of quark diagrams and the possible third-order contribution. Although the calculation accuracy of a_μ^{EW} is more than an order of magnitude lower than that of a_μ^{QED}, the absolute value of its uncertainty is an order of magnitude higher than the measurement error of a_μ.

2.3 Contributions due to strong interactions

The strong interaction contribution to a_μ, although being four orders of magnitude smaller than the electromagnetic contribution, is very significant compared to the experimental errors. This contribution is about 10 times as high as the CERN III experimental error and 100 times as high as the measurement error of a_μ at BNL. Therefore, it is important to calculate a_μ^{had} with a high relative accuracy $\sim 10^{-2}-10^{-3}$.

The main diagrams determining a_μ^{had} are presented in Fig. 6. In the strong interaction contribution, three terms are commonly distinguished: the leading-order (LO) term (from hadron vacuum polarization) $a_\mu^{\mathrm{had,\,LO}}$ (Fig. 6a), the next-to-LO (NLO) term $a_\mu^{\mathrm{had,\,NLO}}$ (Fig. 6b–d), and the LbL term $a_\mu^{\mathrm{had,\,LbL}}$ (Fig. 6e):

$$a_\mu^{\mathrm{had}} = a_\mu^{\mathrm{had,\,LO}} + a_\mu^{\mathrm{had,\,NLO}} + a_\mu^{\mathrm{had,\,LbL}}\,. \tag{22}$$

2.3.1 Contribution due to the hadron vacuum polarization. Due to the smallness of the electromagnetic and weak interaction coupling constants, the perturbation theory enables a high-accuracy calculation of the corresponding contribution. In the case of strong interactions, the perturbation theory is applicable only at high energies where the effective QCD coupling constant becomes small. In calculations of a_μ, the characteristic momentum transfer is of the order of the muon mass, which is significantly smaller than the characteristic energies for asymptotic freedom (about several GeV). Therefore, calculation methods suitable for a_μ^{QED} and a_μ^{EW} are not applicable to the calculation of a_μ^{had}.

A method of calculation of the leading contribution $a_\mu^{\mathrm{had,\,LO}}$ due to hadron vacuum polarization (the diagram in Fig. 6a) based on the use of dispersion relations was proposed in the 1960s [100–103]. To date, it remains the only method that allows achieving the required accuracy.

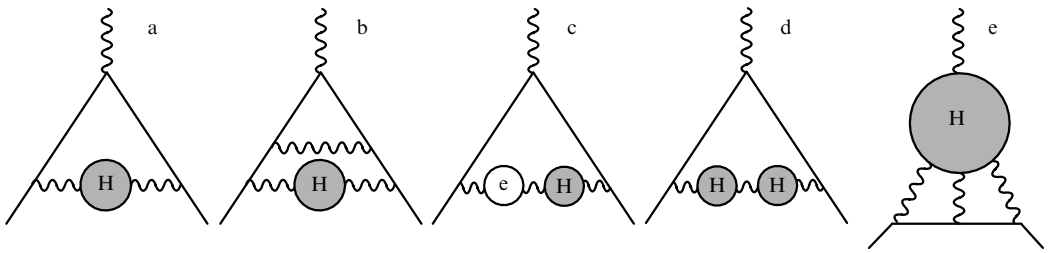

Figure 6. Contributions to the muon anomalous magnetic moment due to strong interactions.

Figure 7. Photon propagator representation as a sum of one-particle-irreducible blocks, each of which has the corresponding polarization operator.

We outline the main steps of the derivation of the key dispersion integral used to calculate $a_\mu^{\mathrm{had,LO}}$. The photon propagator can be represented as a sum of one-particle-irreducible blocks of loop diagrams, none of which can be decomposed into two independent blocks by cutting one photon line (Fig. 7). The contribution from each such block is described by the polarization operator $q^2\Pi'(q^2)$. Adding all contributions yields the photon propagator that takes loop insertions into account:

$$\mathrm{i}D(q^2) = -\frac{\mathrm{i}}{q^2\bigl(1-\Pi'(q^2)\bigr)}\,. \tag{23}$$

Keeping only one irreducible block (as in the diagram in Fig. 6a), we obtain

$$\mathrm{i}D(q^2) = -\frac{\mathrm{i}}{q^2}\bigl(1+\Pi'(q^2)\bigr)\,. \tag{24}$$

The analytic properties of $\Pi(s)$ following from the causality principle allow writing the dispersion relation as

$$-\frac{\Pi'(q^2)}{q^2} = \int_0^\infty \frac{\mathrm{d}s}{s}\,\frac{1}{\pi}\,\mathrm{Im}\,\Pi'(s)\,\frac{1}{q^2-s}\,. \tag{25}$$

Formula (25) can be interpreted as follows: the part $-\Pi'(q^2)/q^2$ of photon propagator (24) corresponding to vacuum polarization is equivalent to the sum of contributions due to massive photons $m_\gamma^2 = s$ with the propagator $1/(q^2-s)$ integrated with the weight $\mathrm{Im}\,\Pi'(s)/(\pi s)$.

The contribution to a_μ from the diagram with a massive photon exchange, $m_\gamma^2 = s$, was calculated in [18, 104]:

$$\begin{aligned} a_\mu^{m_\gamma^2=s} &= \frac{\alpha}{\pi}\,K_\mu(s)\,, \quad \text{where} \\ K_\mu(s) &= \int_0^1 \mathrm{d}x\,\frac{x^2(1-x)}{x^2+(s/m_\mu^2)(1-x)}\,. \end{aligned} \tag{26}$$

Using integral representation (25) for the photon propagator, it is possible to calculate the contribution of vacuum polarization to the muon anomalous magnetic moment of the muon as a sum of contributions due to massive photon exchange (26) integrated with the weight $\mathrm{Im}\,\Pi'(s)/(\pi s)$:

$$a_\mu^{\mathrm{VP}} = \frac{\alpha}{\pi}\int_0^\infty \frac{\mathrm{d}s}{s}\,\frac{1}{\pi}\,\mathrm{Im}\,\Pi'(s)\,K_\mu(s)\,. \tag{27}$$

The optical theorem, which results from the scattering matrix unitarity, allows relating the imaginary part of the polarization operator to the total cross section of particle production in electron–positron annihilation (Fig. 8):

$$\mathrm{Im}\,\Pi'(s) = \frac{\alpha s}{4\pi|\alpha(s)|^2}\,\sigma(\mathrm{e}^+\mathrm{e}^-\to\gamma^*\to\text{anything})(s)\,. \tag{28}$$

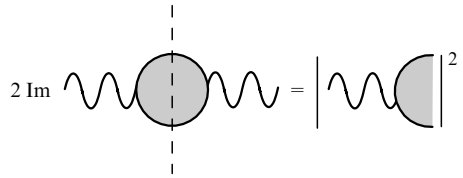

Figure 8. Illustration of the optical theorem.

Contributions of both lepton and hadron vacuum polarizations are included in the polarization operator $\Pi'(s)$. The contribution due to hadron loops has already been taken into account in the calculation of the electromagnetic contribution. When calculating the contribution due to strong interactions in the leading order (see the diagram in Fig. 6a), only the hadron vacuum polarization has to be taken into account. Hence, we finally obtain the formula for $a_\mu^{\mathrm{had,LO}}$

$$a_\mu^{\mathrm{had,LO}} = \frac{\alpha^2}{3\pi^2}\int_{4m_\pi^2}^\infty \frac{\mathrm{d}s}{s}\,R(s)\,K_\mu(s)\,, \tag{29}$$

where $R(s)$ is the normalized total hadron production cross section in electron–positron annihilation:

$$R(s) = \frac{\sigma(\mathrm{e}^+\mathrm{e}^-\to\gamma^*\to\text{hadrons})(s)}{4\pi|\alpha(s)|^2/(3s)}\,. \tag{30}$$

We often use other equivalent expressions for $R(s)$:

$$\begin{aligned} R(s) &= \frac{\sigma(\mathrm{e}^+\mathrm{e}^-\to\text{hadrons})}{\sigma(\mathrm{e}^+\mathrm{e}^-\to\mu^+\mu^-)}\,, \\ \sigma(\mathrm{e}^+\mathrm{e}^-\to\mu^+\mu^-) &= \frac{4\pi|\alpha(s)|^2}{3s}\,, \end{aligned} \tag{31}$$

or

$$\begin{aligned} R(s) &= \frac{\sigma^0(\mathrm{e}^+\mathrm{e}^-\to\text{hadrons})}{\sigma^0(\mathrm{e}^+\mathrm{e}^-\to\mu^+\mu^-)}\,, \\ \sigma^0(\mathrm{e}^+\mathrm{e}^-\to\mu^+\mu^-) &= \frac{4\pi\alpha^2}{3s}\,. \end{aligned} \tag{32}$$

Formula (29) can be rewritten in the form

$$a_\mu^{\mathrm{had,LO}} = \left(\frac{\alpha m_\mu}{3\pi}\right)^2\int_{4m_\pi^2}^\infty \frac{\mathrm{d}s}{s^2}\,R(s)\,\hat{K}(s) \tag{33}$$

with the redefined convolution kernel

$$\hat{K}(s) = \frac{3s}{m_\mu^2}\,K_\mu(s)$$

which is a slowly varying monotonic function asymptotically tending to unity (Fig. 9). It is in this form that this expression is most frequently used in the literature.

Formula (33) allows calculating $a_\mu^{\mathrm{had,LO}}$ using a known $R(s)$. Equation (33) was obtained from the fundamental assumptions of causality and unitarity; therefore, it can be considered exact in the relevant order of perturbation theory. However, it is important to understand how $R(s)$ is related to the observed cross sections. The above derivation suggests that $R(s)$ corresponds to all diagrams in which the virtual photon decays into one or more hadrons and an arbitrary number of other particles. Some important

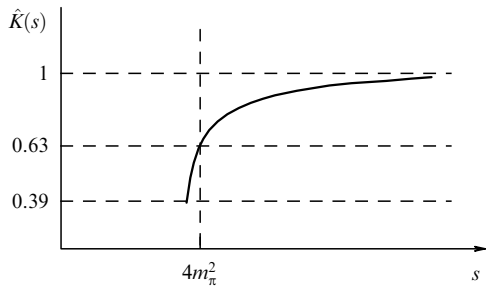

Figure 9. Kernel $\hat{K}(s)$ in dispersion relation (33) [45].

remarks about the relation of $R(s)$ to observed cross sections can be made here.

• Both definitions, (31) and (32), use the muon production cross section $\sigma(e^+e^- \to \mu^+\mu^-)$ in the $m_\mu = 0$ limit. When the real muon cross section is used, the term compensating a change in the phase space must be added.

• $R(s)$ corresponds to the hadron production via one virtual photon. Processes with several photon exchanges or photon emission by initial particles should not be taken into account in $R(s)$; however, they cannot be completely excluded from the observed processes using selection criteria. Therefore, the observed hadron production cross sections should be supplemented with radiative corrections, which are known to an accuracy of 0.1–1%. Processes with photon emission by final hadrons should be taken into account in $R(s)$.

• $R(s)$ corresponds to one-particle-irreducible insertions in the photon propagator, and therefore hadron production should proceed via one virtual photon without loop insertions. In the observed process $e^+e^- \to \gamma^* \to$ hadrons, the virtual photon is described by the full propagator with the vacuum polarization taken into account. Therefore, the vacuum polarization contribution should be excluded from the observed cross section.

The measured hadron cross sections are typically normalized to the Bhabha cross section of $e^+e^- \to e^+e^-$. In this case, definition (32) is actually used. The observed number of events is normalized to the Bhabha scattering cross section calculated with all possible corrections. The obtained hadron production cross section is corrected for the emission of real photons, and the vacuum polarization contribution $|\alpha(s)/\alpha|^2$ is subtracted. The obtained bare cross section $\sigma^0(e^+e^- \to \text{hadrons})$ is used to calculate $R(s)$. Another possibility is to normalize hadron cross sections to the cross section of $e^+e^- \to \mu^+\mu^-$. In this case, it is necessary to add corrections for the emission of real photons, but the vacuum polarization contribution is automatically canceled.

The dependence $\alpha(s)$ can be obtained from Eqn (23) and the normalization condition as $s \to 0$ [105]:

$$\alpha(s) = \frac{\alpha}{1-\Delta\alpha(s)}\,, \quad \Delta\alpha(s) = 4\pi\alpha\,\mathrm{Re}\left(\Pi'(s) - \Pi'(0)\right). \quad (34)$$

However, in this case, both lepton Π'_l and hadron Π'_h contributions to the polarization operator must be taken into account:

$$\Pi'(s) = \Pi'_\mathrm{l}(s) + \Pi'_\mathrm{h}(s)\,. \quad (35)$$

The lepton contribution is calculated using perturbation theory, and to calculate the hadron contribution, a dispersion relation similar to (29) is used:

$$\Delta\alpha_\mathrm{had}(s) = \Pi'_\mathrm{h}(s) - \Pi'_\mathrm{h}(0) = -\frac{\alpha s}{3\pi}\int_0^\infty \frac{R(s')}{s'(s-s'-\mathrm{i}0)}\,\mathrm{d}s'\,. \quad (36)$$

The dependence $\alpha(s)$ in the energy range below 1 GeV was recently measured [106] and found to be in agreement with model (36).

In the low-energy range, experimental data can only be used to calculate $R(s)$; there is no other means to calculate this quantity from first principles. In the high-energy range, the situation is the opposite: $R(s)$ can be calculated using perturbative QCD [107], enabling a higher precision than in the existing experiments. Therefore, in calculating $a_\mu^{\mathrm{had,LO}}$, integral (33) is split into two parts:

$$a_\mu^{\mathrm{had,LO}} = \left(\frac{\alpha m_\mu}{3\pi}\right)^2 \int_{4m_\pi^2}^{E_\mathrm{cut}^2} \frac{\mathrm{d}s}{s^2}\, R_\mathrm{exp}(s)\,\hat{K}(s) + \left(\frac{\alpha m_\mu}{3\pi}\right)^2 \int_{E_\mathrm{cut}^2}^{\infty} \frac{\mathrm{d}s}{s^2}\, R_\mathrm{pQCD}(s)\,\hat{K}(s)\,, \quad (37)$$

where E_cut is the energy above which the calculated value of $R(s)$ is used. The energy E_cut varies in different calculations. For example, in the recent calculation in [44], the computed value of $R(s)$ is used in the energy range 1.8–3.7 GeV and above 5.0 GeV.

In the described method, the calculation of $a_\mu^{\mathrm{had,LO}}$ reduces to measuring the hadron creation cross section from e^+e^- annihilation. Direct measurements are carried out at e^+e^- colliders. In the region of relatively high energies, $\sqrt{s} \gtrsim (1.8-2)$ GeV, inclusive measurements of the cross section σ ($e^+e^- \to$ hadrons) are carried out (see, e.g., [108–111]), in which any nonzero number of hadrons can be identified in the final state (in other words, $R(s)$ is measured directly). At lower energies, a low particle multiplicity does not allow a high-precision detection efficiency: it becomes significantly different for different final states. At the same time, in this energy range, a higher measurement accuracy is required due to an increase in the integrand in (33) at small s. Therefore, in the energy range $\sqrt{s} \lesssim 2$ GeV, the exclusive measurement of cross sections of each separate final hadron state $e^+e^- \to 2\pi, 3\pi, 4\pi, 2\mathrm{K}, \ldots$ is mainly used, and $a_\mu^{\mathrm{had,LO}}$ is calculated as a sum of contributions due to individual final hadron states:

$$a_\mu^{\mathrm{had,LO}} = \sum_{X=\pi^0\,\gamma,\,\pi^+\pi^-,\ldots} a_\mu^{X,\mathrm{LO}} = \sum_X \left(\frac{m_\mu}{3\pi}\right)^2 \int \frac{\mathrm{d}s}{s}\,\frac{3}{4\pi}\,\sigma^0(e^+e^- \to X)\,(s)\,\hat{K}(s)\,. \quad (38)$$

Table 2 shows the contributions to $a_\mu^{\mathrm{had,LO}}$ from principal hadron channels in the energy range up to 1.8 GeV according to [45]. The major contribution to $a_\mu^{\mathrm{had,LO}}$, about 3/4, is due to the process $e^+e^- \to \pi^+\pi^-$, which is due to both the large value of the cross section because of the $\rho(770)$ resonance and an increase in the integrand in (38) as $1/s$. The next-to-leading contributions are due to vector resonances $\omega(782)$ and $\varphi(1020)$ and the process $e^+e^- \to 4\pi$. In general, the contribution due to the energy range $\sqrt{s} < 2$ GeV amounts to about 93% of the total value of $a_\mu^{\mathrm{had,LO}}$. Therefore, measurements of the exclusive cross sections $e^+e^- \to$ hadrons at low energies,

Table 2. Contribution to dispersion integral (33) from the main channels of $e^+e^- \to$ hadrons in the energy range 0.318 GeV $\leqslant \sqrt{s} \leqslant$ 2 GeV. (Data from [45].)

Final state (X)	Contribution to integral (33), $\times 10^{10}$	Fraction in $a_\mu^{\mathrm{had,LO}}$, %
$\pi^0\gamma$	4.00 ± 0.16	0.58
$\pi^+\pi^-$	502.16 ± 2.44	73.10
$\pi^+\pi^-\pi^0$	44.32 ± 1.48	6.45
$\pi^+\pi^-\pi^0\pi^0$	19.69 ± 2.32	2.87
$\pi^+\pi^-\pi^+\pi^-$	14.80 ± 0.36	2.15
K^+K^-	21.99 ± 0.61	3.20
K_SK_L	13.10 ± 0.41	1.91

in particular, the precise measurement of the cross section of $e^+e^- \to \pi^+\pi^-$, play the key role in determining $a_\mu^{\mathrm{had,LO}}$.

The first measurements of hadron cross sections and determinations of the parameters of vector resonances ρ, ω, and φ were carried out at the e^+e^- colliders VEPP-2 in Novosibirsk [112] and ACO (Anneau de Collision d'Orsay) (France) [113–115]. These measurements enabled an estimation of $a_\mu^{\mathrm{had,LO}}$ to a 10% uncertainty [102, 103], corresponding to the experimental errors of a_μ in the CERN III experiment.

Most of the e^+e^- colliders constructed in different laboratories around the world were designed to carry out high-energy experiments. For a long time, VEPP-2M was the only e^+e^- collider capable of working at low energies. On this collider, which operated from 1975 until 2000, a series of measurements of hadron cross sections was performed at low energies $\sqrt{s} < 1.4$ GeV. The first significant step toward increasing the accuracy of $a_\mu^{\mathrm{had,LO}}$ to $\approx 2\%$ was made due to hadron cross section measurements in the OLYA, CMD [116], and ND (neutral detector) [117] experiments with the VEPP-2M collider, in particular, measurements of the cross section of $e^+e^- \to \pi^+\pi^-$ [118]. However, this was insufficient to reach an accuracy of about 0.8%, corresponding to the experimental uncertainty in a_μ at BNL. Two experiments, CMD-2 [33] and SND [34], which started taking data in 1993 and 1996, performed a series of hadron cross section measurements at energies up to 1.4 GeV (Fig. 10), most of which remain the most precise direct measurements to date. In particular, measurements of the $e^+e^- \to \pi^+\pi^-$ cross section with the CMD-2 detector [119–123] achieved an accuracy better than 1%.

VEPP-2M completed operation in 2001. In its place, construction of the VEPP-2000 collider [35] with a wider working energy range up to 2 GeV and an order-of-magnitude higher luminosity began. Two detectors, CMD-3 [36] and upgraded SND [37], started running in 2010. Measurements of the $e^+e^- \to$ hadrons cross sections are one of the principal goals of the experiments. Results for several final states have already been published [38].

Even the hadron cross sections measured at VEPP-2M, the calculation uncertainty of $a_\mu^{\mathrm{had,LO}}$ was worse than expected (and achieved) for a_μ at BNL. This stimulated the search for alternative tools for measuring the cross sections $e^+e^- \to$ hadrons, in addition to direct measurements. The first of such tools was based on the analysis of spectra of hadron decays of the τ lepton [124]. In the Standard Model, interaction vertices of W and γ with a pair of quarks are strongly related. Under the assumption of the isospin symmetry, the decay $\tau^- \to \pi^-\pi^0\nu_\tau$ can be related to the $e^+e^- \to \pi^+\pi^-$ cross section (Fig. 11): the spectral function $v_{1,\pi^-\pi^0}(s)$ representing the normalized mass distribution in the τ decay,

$$v_{1,\pi^-\pi^0}(s) = \frac{m_\tau^2}{6|V_{ud}|^2 S_{\mathrm{EW}}} \frac{\mathrm{Br}(\tau^- \to \pi^-\pi^0\nu_\tau)}{\mathrm{Br}(\tau^- \to e^-\nu_\tau\bar{\nu}_e)} \times \frac{\mathrm{d}N_{\pi^-\pi^0}}{N_{\pi^-\pi^0}\,\mathrm{d}s} \left[\left(1 - \frac{s}{m_\tau^2}\right)^2 \left(1 + \frac{2s}{m_\tau^2}\right)\right]^{-1}, \quad (39)$$

is related to the isovector component of the $e^+e^- \to \pi^+\pi^-$ cross section as

$$\sigma^{I=1}(e^+e^- \to \pi^+\pi^-)(s) = 4\pi\alpha^2 s\, v_{1,\pi^-\pi^0}(s)\,. \quad (40)$$

Here, V_{ud} is the Cabibbo–Kobayashi–Maskawa (CKM) matrix describing transitions between u and d quarks, and $N_{\pi^-\pi^0}$ is the number of $\tau^- \to \pi^-\pi^0\nu_\tau$ events. The factor S_{EW} is needed to take electroweak radiative corrections into account [125]. Initially, the hadron cross sections that were known with better accuracy were used to predict the spectral

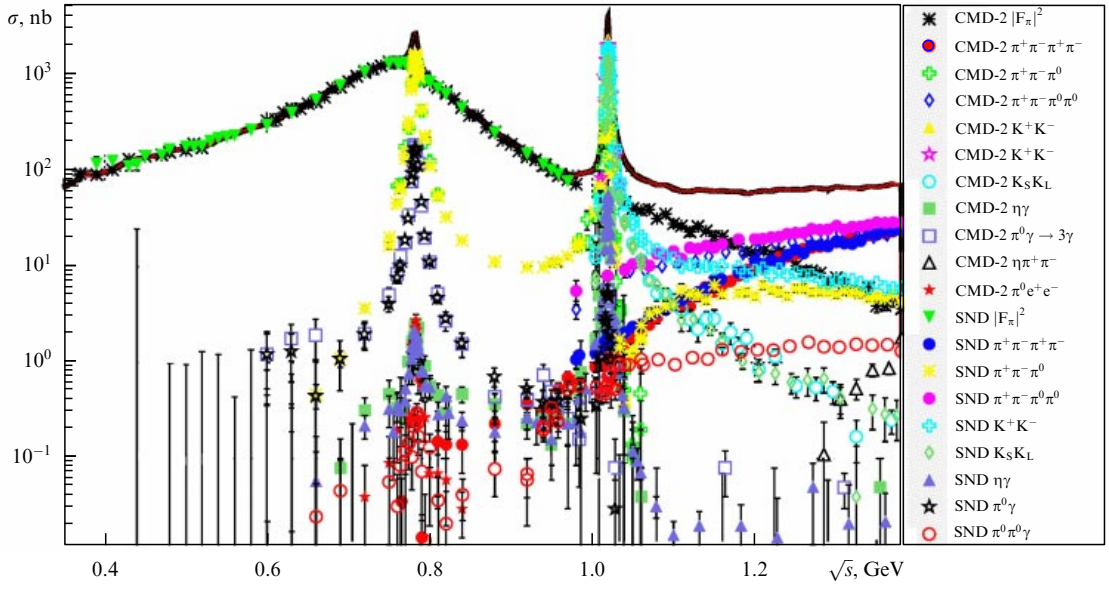

Figure 10. (Color online.) Hadron cross section measured in the CMD-2 and SND experiments using the VEPP-2M collider.

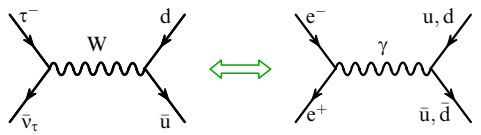

Figure 11. Relation of the decay $\tau^- \to \pi^-\pi^0\nu_\tau$ to the $e^+e^- \to \pi^+\pi^-$ cross section.

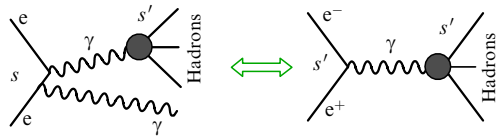

Figure 12. (Color online.) Initial-state radiation method.

functions and relative probabilities of hadron τ decays [126]. However, precise measurements of the spectral functions in the ALEPH experiment [127] make it possible to reverse the situation and to use these data to improve the hadron cross sections. This approach was first implemented in [128], and the accuracy of $a_\mu^{\mathrm{had,LO}}$ was improved at that time from 2.2% (e^+e^- only) to 1.3% ($e^+e^- + \tau$). This calculation took the corrections due to isospin symmetry breaking into account: the presence of the isoscalar component of the $e^+e^- \to$ hadrons cross section, the mass difference between π^0 and $\pi^\pm$, and the emission of photons by final-state particles.

With the appearance of more accurate measurements of the $e^+e^- \to \pi^+\pi^-$ cross sections in the CMD-2 and SND experiments and ISR measurements (to be discussed below), it became clear that there is a systematic difference between direct measurements of hadron cross sections and their predicted values from τ decays. In terms of $a_\mu^{\mathrm{had,LO}}$, the difference was 1.5–2%, which exceeded the accuracy in the BNL experiments. The appearance of new measurements of spectral functions [129] has not fundamentally changed the situation.

The discrepancy between the τ and e^+e^- data persisted for more than 10 years, until it was shown in [130] that an additional correction related to the isospin symmetry breaking due to $\gamma-\rho$ mixing must be taken into account. This correction fully compensated the systematic difference between the τ and e^+e^- data. In spite of resolving the problem with this difference, the τ data are not presently used to calculate $a_\mu^{\mathrm{had,LO}}$, because of both the appearance of many new collider measurements of hadron cross sections and the impossibility of accurately taking the isospin symmetry breaking corrections into account.

New data were obtained using the initial-state radiation (ISR) measurements of hadron cross sections. The idea of the method [131–135] is to infer the energy dependence of the $\sigma(e^+e^- \to X)(s)$ cross section from the invariant mass spectrum of a hadron system X in the process $e^+e^- \to X + \gamma$, where the photon is emitted by one of the initial particles (Fig. 12):

$$\frac{\mathrm{d}\sigma(e^+e^- \to X + \gamma)(s, s')}{\mathrm{d}\sqrt{s'}} = \frac{2\sqrt{s'}}{s}\,\varepsilon(s, s')\,W(s, x)\,\sigma^0(e^+e^- \to X)(s')\,, \qquad (41)$$

where $\sqrt{s}$ is the e^+e^- energy in the center-of-mass system (c.m.s), $\sqrt{s'}$ is the c.m.s. hadron system energy, and $\varepsilon(s, s')$ is the detection efficiency. The radiator function $W(s, x)$ describing the probability of emission of a photon carrying the fraction $x = 1 - s'/s$ of the initial energy can be calculated in QED with radiative corrections [134].

An advantage of the ISR method is that the accumulation of statistics is performed with a constant energy $\sqrt{s}$ of beams at the collider: the scanning of the available energy range $\sqrt{s'} < \sqrt{s}$ is done automatically due to the detection of events with different energies carried away by the emitted photon. A disadvantage is that the detection cross section of the process $e^+e^- \to X + \gamma$ is 2 to 3 orders of magnitude smaller than that of the $e^+e^- \to X$ process due to an additional radiation vertex $\sim \alpha$. The ISR measurements became possible due to the appearance of new high-luminosity colliders: BaBar [39] and Belle [40] B-factories and KLOE [41, 42] φ-factory. The construction of these colliders does not allow scanning wide energy ranges; however, their luminosity in a narrow region near the energy $\Upsilon(4S)$ for the B-factory and $\varphi(1020)$ for the φ-factory is several orders of magnitude higher than that of the previous generation of colliders.

The most detailed measurement by the ISR method was done in the BaBar experiment [43] (Fig. 13). Since the publication of review [43], more than 10 additional exclusive channels have been measured, which are not shown in Fig. 13. All exclusive channels probed earlier by VEPP-2M were typically measured with a larger statistics and in a wider energy range. In addition, a great number of modes with a significant cross section beyond 1.4 GeV unavailable for VEPP-2M were measured.

In the BaBar experiment [135, 136], the leading cross section of $e^+e^- \to \pi^+\pi^-$ was measured with a record-high systematic accuracy of 0.5%. A series of measurements of the $e^+e^- \to \pi^+\pi^-$ cross section was performed in the KLOE experiment [137–139]. Because the initial c.m.s. energy in this experiment was about 1 GeV, the measurements were performed only for energies below 1 GeV. The KLOE experiment enabled the comparison of three measurement methods: with radiation photon detection, without photon detection, and with normalization to the $e^+e^- \to \mu^+\mu^-\gamma$ process. Quite recently, measurement of the pion formfactor by the ISR method in the BES III (Beijing Spectrometer) experiment [140] has been reported.

Presently, the statistics on hadron cross section measurements by the ISR method are much larger than those from direct VEPP-2M measurements. However, a detailed comparison, which is possible only for the $e^+e^- \to \pi^+\pi^-$ cross section measured with a high accuracy in several experiments, shows that there are differences between the measurement results beyond the claimed systematic errors. It is currently unclear whether these differences are due to underestimated systematic experimental errors or to more fundamental limitations of the ISR method (for example, related to the incorrect description of the radiator function). We note that a similar radiator function is used to calculate radiative corrections in direct hadron cross section measurements. However, in direct measurements, the main effect is determined by low x, whereas in the IRS measurements, it is determined by high x.

The history of $a_\mu^{\mathrm{had,LO}}$ calculations includes dozens of papers differing by the experimental data used, their unification method, the energy range of calculations by perturbative

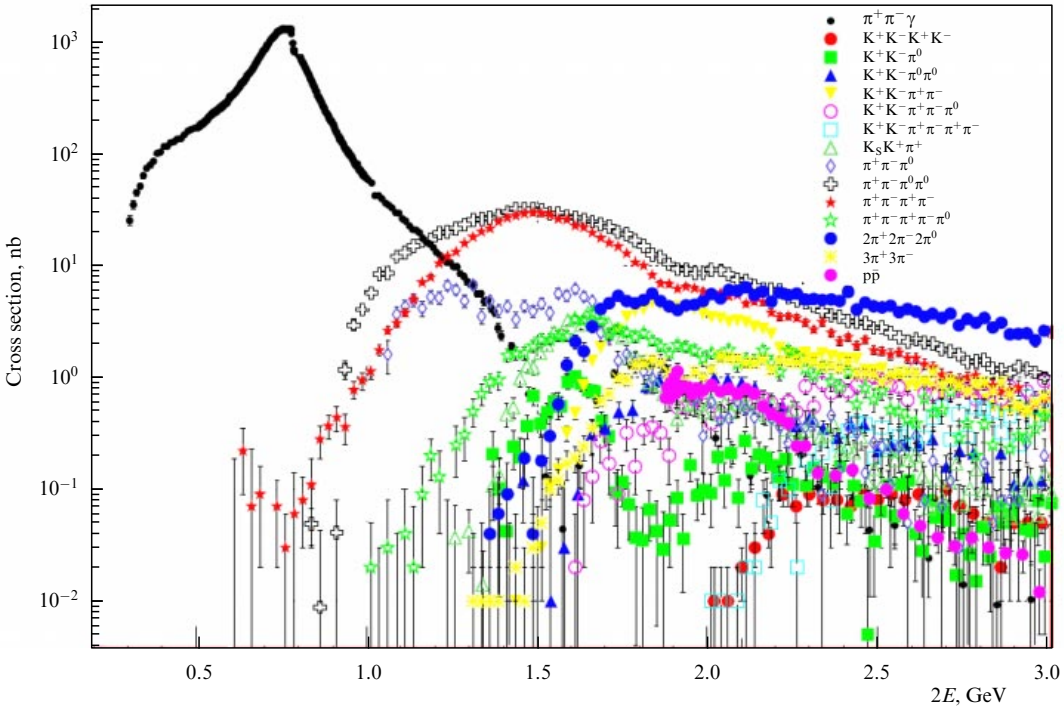

Figure 13. (Color online.) Hadron cross sections as measured by the initial-state radiation method in the BaBar experiment. (From [43].)

QCD (pQCD), etc.

Figure 14 shows a retrospective comparison of the results of the best known calculations. It is easily seen how the accuracy increased in the 2000s when new hadron cross section measurements became available from the CMD-2, SND, BaBar, and KLOE experiments. Currently, to calculate $a_\mu^{\text{had, LO}}$, only e^+e^- data obtained by both the energy scanning method (CMD-2, SND) and the ISR method (BaBar, KLOE, BES-III) are used. The total experimental error increases due to a factor taking systematic deviations between the measurements into account. The integration is performed in a model-independent way (for example, by the method of trapezoids). Such an approach was first accurately used in [141]. In previous works, for example, in [144] in 1990 (with the result of this paper presented in Fig. 14 among others), the hadron cross sections were approximated by a function that was subsequently used to calculate the dispersion integral. Although this approach allowed decreasing the statistical error, it led to the appearance of an uncontrolled model error.

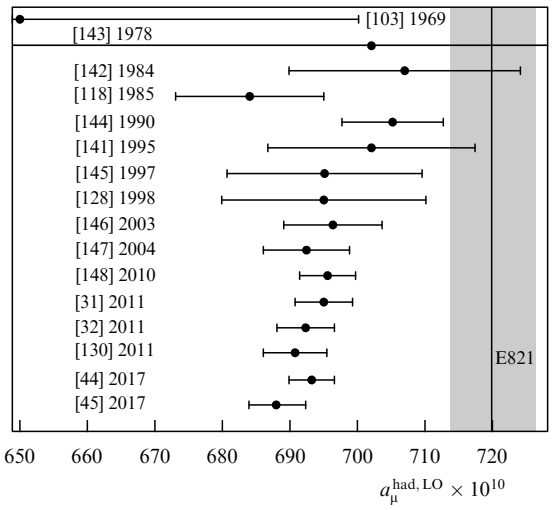

Figure 14. Review of the calculations of the leading-order contribution due to strong interactions $a_\mu^{\text{had, LO}}$. Presented are data from [31, 32, 44, 45, 103, 118, 128, 141–148]. The shaded strip shows the difference between the most precise measurement of a_μ (in the E821 experiment) and the sum of all contributions in the Standard Model except $a_\mu^{\text{had, LO}}$.

The results of the latest estimates of $a_\mu^{\text{had, LO}}$ in [44, 45] that take all existing data into account give

$$a_\mu^{\text{had, LO}} = (693.1 \pm 3.4) \times 10^{-10} \quad (0.49\%)\,, \tag{42}$$

$$a_\mu^{\text{had, LO}} = (688.07 \pm 4.14) \times 10^{-10} \quad (0.60\%)\,. \tag{43}$$

Despite a number of measurements of the $e^+e^- \to \pi^+\pi^-$ cross section with an accuracy better than 1%, this channel makes the main contribution to the error of $a_\mu^{\text{had, LO}}$, about 0.35–0.4%. The next important error contribution is due to the channel $e^+e^- \to \pi^+\pi^-\pi^0\pi^0$. The smaller error in (42) is primarily due to the preliminary measurements of the $e^+e^- \to \pi^+\pi^-\pi^0\pi^0$ cross section by the ISR method in the BaBar experiment.

Hadron cross section measurements in the ongoing CMD-3 and SND experiments [38] will play an important role in further decreasing the error in determining $a_\mu^{\text{had, LO}}$. Thanks to the high luminosity of the VEPP-2000 collider, the statistics in both experiments are several times larger than those in the ISR experiments. This will enable a detailed matching of the direct measurements of the hadron cross section energy dependence with the ISR measurements, which can possibly resolve the observed discrepancies. Moreover, the rich statistics allow experimental tests of the models used in the calculation of radiative corrections in direct measurements and of the radiator function in the ISR method.

Thanks to the fast increase in computer power, it has become possible to determine $a_\mu^{\text{had, LO}}$ by a totally independent method using QCD lattice calculations. In fact, this method enables calculations of $a_\mu^{\text{had, LO}}$ from first principles without the use of experimental data. To date, an accuracy of 1.5–2% has been reached [149–151], and the obtained results are consistent with calculations based on the use of the dispersion integral. It is expected that already in this decade, the calculation accuracy will be better than 1%.

Presently, $a_\mu^{\text{had, LO}}$ is determined with an accuracy of about 0.5%. In the next few years, a significant accuracy increase in the direct measurement of hadron cross sections and in lattice calculations is expected. This gives rise to three independent methods for calculating $a_\mu^{\text{had, LO}}$, each with an accuracy of the order of or better than 0.5%: the method using the direct hadron cross section measurements, ISR measurements, and first-principle lattice calculations. This will make it possible, on the one hand, to increase the calculation accuracy, which is needed in relation to the new measurements of a_μ at Fermilab (USA), and, on the other hand, to check the reliability of the calculations at this accuracy level.

2.3.2 Next-to-leading-order contribution. The contribution to the muon anomalous magnetic moment due to strong interactions in the next-to-leading order of the perturbation theory, $a_\mu^{\text{had, NLO}}$, is defined by diagrams shown in Fig. 6b–d. The LbL scattering term $a_\mu^{\text{had, LbL}}$ described by the diagram shown in Fig. 6e, although appearing in the same order, is considered separately in Section 2.3.3.

The contribution due to diagrams presented in Fig. 6b–d can be calculated using the dispersion relations. Here, integrals similar to (33) arise, but with other kernel functions. For the first time, an estimate of the contribution due to strong interactions in the next-to-leading order was obtained in [142]. More accurate calculations were carried out in [152]. Subsequent series of calculations [31, 128, 147] confirmed this result and improved its accuracy, mainly due to new measurements of $R(s)$. The result of one of the calculations [31] is

$$a_\mu^{\text{had, NLO}} = (-9.84 \pm 0.06_{\text{exp}} \pm 0.04_{\text{rad}}) \times 10^{-10}\,. \qquad (44)$$

As in the case of the leading-order contribution, the calculation accuracy of $\sim 1\%$ is mainly determined by the calculation accuracy of $R(s)$. Due to the smallness of the contribution itself (about 1.5% of $a_\mu^{\text{had, LO}}$), the accuracy of determining $a_\mu^{\text{had, NLO}}$ does not significantly contribute to the total calculation error of a_μ^{had}.

Quite recently, the first estimates of the next-to-next-to-leading contribution were obtained [153, 154]:

$$a_\mu^{\text{had, NNLO}} = (1.24 \pm 0.01) \times 10^{-10}\,. \qquad (45)$$

Although this contribution is much larger than one could expect from the naive scaling $a_\mu^{\text{had, NLO}}/a_\mu^{\text{had, LO}} \approx 1/70$, a good convergence of the perturbation theory series is observed.

2.3.3 Light-by-light scattering contribution. Calculating the LbL scattering contribution, $a_\mu^{\text{had, LbL}}$, which arises in the next-to-leading order (the diagram in Fig. 6e), is the most difficult. The calculation of the electromagnetic contribution to a_μ shows that such LbL scattering diagrams can be logarithmically enhanced and provide the leading contribution in the corresponding order of the perturbation theory. The value of $a_\mu^{\text{had, LbL}}$ cannot be calculated nor related to experimental data using dispersion relations. The calculation results turn out to be model dependent, which leads to a rather high uncertainty.

The calculation of $a_\mu^{\text{had, LbL}}$ is a very active and extensive topic of theoretical studies, which is beyond the scope of this review. The calculation details can be found in reviews [45, 155] and the references therein. In this section, we briefly discuss the state-of-the-art in this field.

The calculation of $a_\mu^{\text{had, LbL}}$ was carried out in the 1990s independently by two groups: [156–158] and [159, 160]. Further development of the calculation method was proposed in [161–163]. The last group found some errors and shortcomings in the initial calculations. In particular, it was noted that both groups independently obtained wrong sign when calculating the leading contribution due to the pseudoscalar meson exchange. The result of the initial calculations was used to compare the first measurements of a_μ at BNL [164] with the Standard Model predictions. After correcting the sign in the calculations, the discrepancy between the measured and calculated values decreased by almost a factor of two.

In these calculations, effective models are used in which the hadron block in the diagram in Fig. 6e consisting of quarks and gluons is substituted by an exchange by different hadrons. The main contribution to $a_\mu^{\text{had, LbL}}$ is due to the exchange by pseudoscalar mesons π^0, η, and η', which corresponds to the diagram shown in Fig. 15a. In addition, the calculations take exchanges by 0^{++} mesons (a_0, f_0, and f_0'), 1^{++} mesons (a_1, f_1, and f_1'), 2^{++} mesons (a_2 and f_2), and diagrams with pion loops into account (Fig. 15b). In the high-momentum region, the contribution due to quarks and not hadron loops is taken into account. To illustrate the amplitude of different contributions, we give the results of calculations in [45]:

$$\begin{aligned} a_\mu^{\text{had, LbL}} = \big[& \underbrace{9.545(6.468 + 1.487 + 1.590) \pm 1.240}_{(\pi^0, \eta, \eta')} \\ & + \underbrace{0.755(0.189 + 0.519 + 0.047) \pm 0.271}_{(a_1, f_1, f_1')} \\ & - \underbrace{0.598(-0.017 - 0.296 - 0.285) \pm 0.120}_{(a_0, f_0, f_0')} \\ & + \underbrace{0.11(0.079 + 0.007 + 0.022 + 0.002) \pm 0.01}_{(f_2', f_2, a_2', a_2)} \\ & - \underbrace{2.0 \pm 0.5}_{(\pi\text{-loop})} + \underbrace{2.23 \pm 0.4}_{(\text{quark loop})} + \underbrace{0.3 \pm 0.2}_{(\text{NLO})} \big] \times 10^{-10} \\ = {} & (10.34 \pm 2.88) \times 10^{-10}\,. \end{aligned} \qquad (46)$$

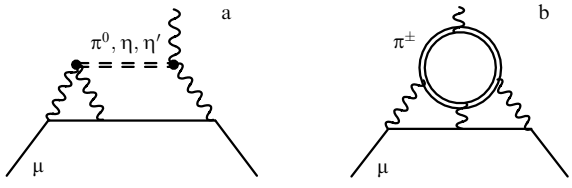

Figure 15. Main diagrams in calculations of $a_\mu^{\text{had, LbL}}$.

This result can be compared to the so-called Glasgow consensus (GC) [165],

$$a_{\mu,\mathrm{GC}}^{\mathrm{had,\,LbL}} = (10.5 \pm 2.6) \times 10^{-10}\,, \tag{47}$$

and to individual calculations, for example, by Jegerlehner and Nyffeler (JN) [166] and Melnikov and Vainshtein (MV) [163]:

$$a_{\mu,\mathrm{JN}}^{\mathrm{had,\,LbL}} = (11.6 \pm 4.0) \times 10^{-10}\,, \tag{48}$$

$$a_{\mu,\mathrm{MV}}^{\mathrm{had,\,LbL}} = (13.6 \pm 2.5) \times 10^{-10}\,. \tag{49}$$

Recently, the first estimates of next-order corrections to $a_\mu^{\mathrm{had,\,LbL}}$ were obtained in [167], which arise in the same order of the perturbation theory as $a_\mu^{\mathrm{had,\,NNLO}}$:

$$a_\mu^{\mathrm{had,\,LbL-NLO}} = (0.3 \pm 0.2) \times 10^{-10}\,. \tag{50}$$

This contribution has already been taken into account in (46).

The main properties of the LbL scattering contribution are well understood. Essentially, except for the error in the sign of the contribution due to pseudoscalar mesons mentioned above, the value of $a_\mu^{\mathrm{had,\,LbL}}$ stays quite stable over the whole history of calculations. The calculation accuracy is determined by the model error; therefore, it is necessary to determine the corresponding model parameters more accurately.

In all calculations based on the effective model, hadron form factors play the key role. In particular, in the case of the π^0 exchange, the transition form factor describes the vertex of the $\pi^0\gamma\gamma$ interaction:

$$\mathcal{M}\left[\pi^0(q) \to \gamma(p_1,\lambda_1)\,\gamma(p_2,\lambda_2)\right] = e^2\varepsilon^{*\mu}(p_1,\lambda_1)\,\varepsilon^{*\nu}(p_2,\lambda_2)\,\epsilon_{\mu\nu\alpha\beta}\,p_1^\alpha p_2^\beta \mathcal{F}_{\pi^{0*}\gamma^*\gamma^*}(q^2,p_1^2,p_2^2), \tag{51}$$

where asterisks mark virtual (off-shell) particles, $\mathcal{M}\,[...]$ is the transition matrix element, q, p_1, p_2 are 4-vectors of the π^0 meson and two photons, λ_1 and λ_2 are the polarizations of the photons, e is the electron charge, $\varepsilon^{*\mu}(p_1,\lambda_1)$ and $\varepsilon^{*\nu}(p_2,\lambda_2)$ are the polarizations, $\epsilon_{\mu\nu\alpha\beta}$ is the totally antisymmetric tensor, and $\mathcal{F}_{\pi^{0*}\gamma^*\gamma^*}(q^2,p_1^2,p_2^2)$ is the transition form factor. In the general case where all particles are virtual, $\mathcal{F}_{\pi^{0*}\gamma^*\gamma^*}(q^2,p_1^2,p_2^2)$ is unobservable. However, in separate kinematic regions, it can be related to experimentally observed quantities, which enables imposing boundary conditions and continuing $\mathcal{F}_{\pi^{0*}\gamma^*\gamma^*}$ into the unobserved region. In particular, the constant $\mathcal{F}_{\pi^0\gamma\gamma}(m_\pi^2,0,0)$ is related to the $\pi^0 \to \gamma\gamma$ decay width, measured with an accuracy better than 3% [168]. Another boundary condition can be obtained by measuring the transition form factor in the two-photon production $e^+e^- \to e^+e^-\pi^0$, which corresponds to the measurement of $\mathcal{F}_{\pi^{0*}\gamma^*\gamma}(m_\pi^2,-q^2,0)$. These measurements were carried out in the CELLO [169], CLEO [170], BaBar [171], and Belle [172] experiments in the range of $-q^2$ from 1 to 35 GeV^2. The KLOE-2 experiment plans to measure the transition form factor of π^0 in the range of small $-q^2$ from 0.01 to 0.1 GeV^2 [173]. Although such measurements are not completely model independent, they allow significantly constraining the admissible parameters of the model used and accordingly decreasing the model uncertainty. Estimates show that improvement by a factor of 2 to 3 can be expected [174].

The lattice QCD calculations offer a model-independent method to determine $a_\mu^{\mathrm{had,\,LbL}}$. Although the accuracy of lattice calculations is still lower than that of effective models, this research avenue has been topical in the last few years [175–179]. One of the recent calculations [178] gives

$$a_\mu^{\mathrm{had,\,LbL}}(\mathrm{LQCD}) = (5.35 \pm 1.36) \times 10^{-10}\,, \tag{52}$$

which is almost half of (47). However, we note that only the statistical error is given here. Systematic errors related to the finite lattice size and other features of the calculations have not been estimated yet.

Another prospect is to use lattice calculations to estimate separate contributions to $a_\mu^{\mathrm{had,\,LbL}}$. In particular, in recent papers [180, 181], lattice calculations have been used to construct the transition form factor $\pi^0 \to \gamma^*\gamma^*$ with two virtual photons $\mathcal{F}_{\pi^{0*}\gamma^*\gamma^*}(m_\pi^2,p_1^2,p_2^2)$, which was later used to calculate the π^0-exchange contribution to $a_\mu^{\mathrm{had,\,LbL}}$. The obtained result

$$a_\mu^{\mathrm{had,\,LbL}}(\pi^0,\mathrm{LQCD}) = (6.50 \pm 0.83) \times 10^{-10} \tag{53}$$

is in good agreement with phenomenological estimates (46).

2.4 Anomalous magnetic moment of the muon in the Standard Model

Combining the contributions due to electromagnetic (15), weak (21), and strong interactions (42), (44)–(46), we obtain the following estimate of the anomalous magnetic moment of the muon in the Standard Model:

$$a_\mu\,(\mathrm{SM}) = 116\,591\,821\,(45) \times 10^{-11} \quad (0.39\,\mathrm{ppm})\,. \tag{54}$$

3. Measurements of the anomalous magnetic moment of the muon

3.1 Experimental measurements of the muon anomalous magnetic moment at CERN

Basic principles of the precision measurements of the anomalous magnetic moment of the muon were realized in a series of experiments carried out at CERN in the 1960s–1970s.

The first measurements of g_μ and a_μ [16, 17] were performed for muons at rest: a muon beam was stopped in a target placed in a uniform magnetic field, and the time dependence of the muon spin direction was measured. The precession frequency of the muon spin

$$\boldsymbol{\omega}_\mathrm{s} = -g_\mu \frac{e\mathbf{B}}{2m} - \frac{e\mathbf{B}}{\gamma m}\,(1-\gamma) \tag{55}$$

is proportional to g_μ for muons at rest ($\gamma = 1$). A very high measurement precision of g_μ [17] (better than 0.01%) enabled only a 10% measurement uncertainty of a_μ due to its relative smallness.

However, in experiments with moving muons, a_μ can be measured directly. In a uniform magnetic field perpendicular to the direction of motion ($\boldsymbol{\beta}\,\mathbf{B} = 0$), a particle moves along a circle with the cyclotron frequency ω_c:

$$\boldsymbol{\omega}_\mathrm{c} = -\frac{e\mathbf{B}}{m\gamma}\,. \tag{56}$$

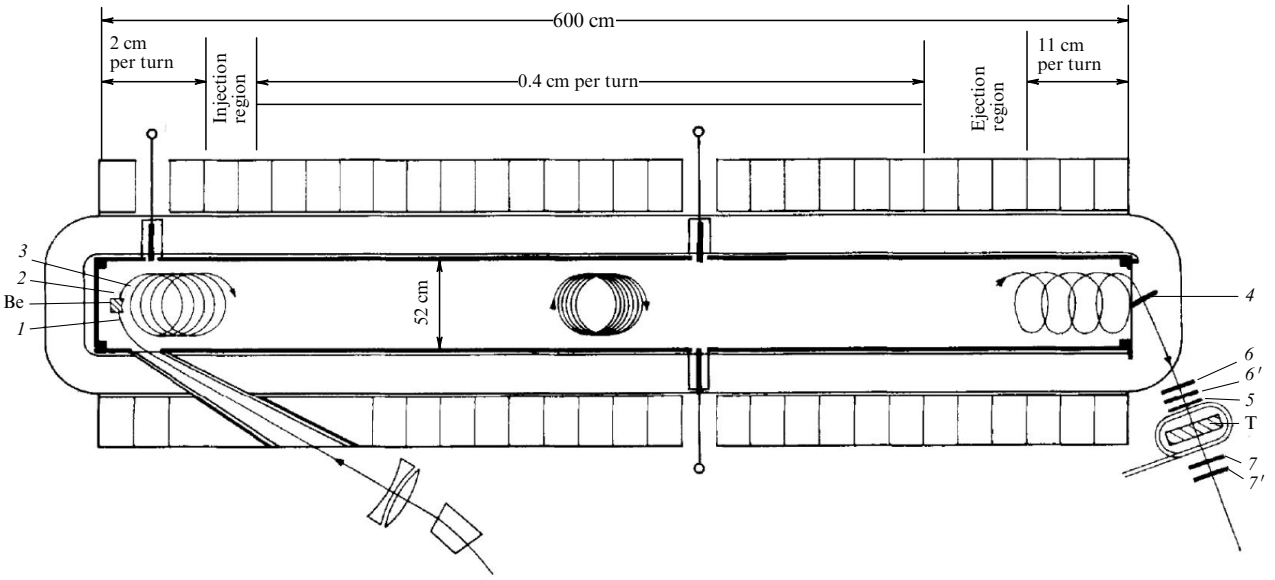

Figure 16. Schematic of the first (CERN I) experiment for measuring a_μ. *1–4* — muon counters, *5–7*, *6′*, *7′* — counters to detect muon-decay electrons. Be — beryllium moderator, T — target for stopping muons.

The difference between the spin precession and cyclotron frequencies

$$\boldsymbol{\omega}_a = \boldsymbol{\omega}_s - \boldsymbol{\omega}_c = -\left(\frac{g-2}{2}\right)\frac{e\mathbf{B}}{m} = -a_\mu \frac{e\mathbf{B}}{m}\,, \tag{57}$$

is proportional to a_μ and is independent of the muon momentum. Therefore, to measure a_μ and not g_μ, it is necessary to measure the muon spin precession frequency relative to its momentum, not in the rest frame.

The first experimental measurement of a_μ using moving muons was carried out at CERN in 1958–1962 (CERN I) [22, 23, 182]. The setup of the experiment is shown in Fig. 16. A 6 m dipole magnet occupied most of the installation. Polarized muons from decays of pions produced in a synchrocyclotron were injected into the magnet to hit a beryllium moderator, where the mean momentum of the muons decreased to ≈ 100 MeV/c. In the magnetic field, muons started moving along a circle. The unique magnetic field structure in the magnet caused circulating muons to drift along the magnet. At the end of the magnet, the muons entered the region with a large gradient of the field and were directed outside to stop in a detector. Because the detector was placed outside the magnetic field, the spin of the stopped muons was 'frozen' at the instant they flew out from the magnet. The muon spin direction in the detector was inferred from the angular anisotropy of the decay electrons. In passing across the magnet, muons made 1000 to 2000 revolutions, which corresponded to about one spin precession period relative to the momentum (one period with a frequency ω_a). The mean counting rate of the decay electrons was approximately 0.25 Hz. The mean field that was 'observed' by the muons over the flight time was about 1.5 T.

The asymmetry of decay electrons as a function of the muon flight time through the magnet is shown in Fig. 17. With this dependence approximated as $A(t) = A\sin(\omega_a t + \varphi_a)$, the final result was obtained: $a_\mu(\text{CERN I}) = (1162 \pm 5) \times 10^{-6}$ with an accuracy of 0.4%, which was by an order of magnitude higher than the most precise measurements for muons at rest. This result definitely confirmed that the muon behaves like a heavy analogue of the electron. Statistical and systematic errors approximately equally contributed to the final uncertainty of the experiment. A further increase in accuracy in the CERN I experiment was almost impossible.

The counting rate of decay electrons in the experiment with moving muons is described by an exponential muon decay superimposed on oscillations with the frequency ω_a:

$$N(t) \sim N(0)\,\exp\left(-\frac{t}{\gamma\tau}\right)\left[1 + A\sin(\omega_a t + \varphi)\right], \tag{58}$$

where $\gamma\tau$ is the lifetime of a moving muon (and τ is the lifetime of a muon at rest), and A is the observed muon polarization depending on the detection method. The statistical measurement error of ω_a (and hence of the anomalous magnetic moment) in experiments measuring $N(t)$ with approximation by the function in (58) is

$$\frac{\delta a_\mu}{a_\mu} \approx \frac{\delta\omega_a}{\omega_a} = \frac{\sqrt{2}}{\omega_a\gamma\tau\sqrt{NA^2}}\,, \tag{59}$$

where N is the total number of decay events.

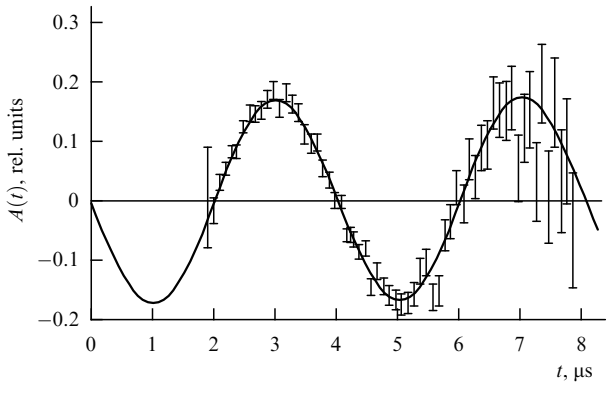

Figure 17. Counting asymmetry of decay electrons as a function of the flight time of a muon through the magnet in the CERN I experiment. The smooth curve shows the fit to the function $A(t) = A\sin(\omega_a t + \varphi_a)$ [23].

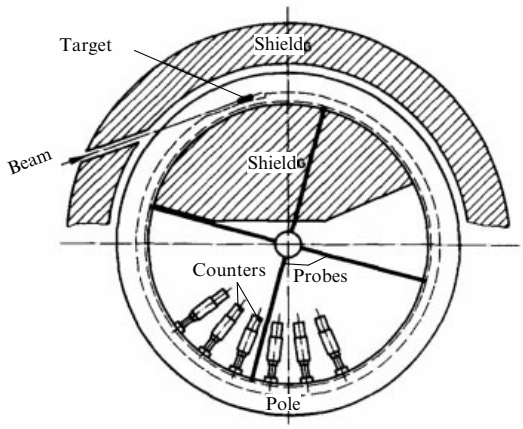

Figure 18. Schematic of the second (CERN II) experiment for measuring a_μ [24].

To improve the accuracy, besides increasing the experimental statistics, it is possible to increase the number of observed precession periods (in the CERN I experiment, only one period was observed). For this, it is necessary to increase either the magnetic field (which increases ω_a) or the muon lifetime by increasing γ. Technically, it is very challenging to increase the magnetic field: the 1.5 T field is close to the maximum possible for large constant-field magnets. Therefore, high-energy muons must be used.

The possibility of using high-energy muons appeared after the Proton Synchrotron (PS) was commissioned. The second experiment to measure a_μ was carried out in 1962–1968 (CERN II) [24]. The general setup of the experiment is shown in Fig. 18. Measurements were performed using muons with the momentum 1.28 GeV/c ($\gamma = 12$, $\gamma\tau = 27$ μs). To store the muons, a storage ring 5 m in diameter was constructed with the mean magnetic field of 1.7 T. To keep muons in the ring during the observation time, which was 200 μs (or 4000 revolutions), a small gradient of the main field was introduced to obtain weak focusing with the field index $n = 0.13$.

To inject a particle beam into an equilibrium orbit in a uniform field, it has to be 'kicked'; otherwise, after one revolution, the beam would collide with the wall. To bypass this difficulty, in the CERN II experiment, muons were not injected into the ring but were produced directly inside it. A proton beam from the PS with a momentum of 10.5 GeV/c was directed onto a target placed in the magnetic field inside the storage ring. The proton beam consisted of 2 to 3 narrow bunches (with a duration of 10 ns) separated by a time interval of 105 ns. The revolution time in the ring was 52.5 ns; therefore. the muons created by different proton bunches formed one common muon bunch. About 70% of the protons interacted in the target to produce pions (in addition to numerous other particles) with a momentum of about 1.3 GeV/c. Around 20% of these pions decayed during one revolution. Muons that flew forward during a pion decay under a small angle went into an equilibrium orbit. The polarization of the initial muon bunch was about 25%, because the muons from pion decays with different momenta and polarizations were also captured in the equilibrium orbit.

In contrast to all previous experiments, the particles in CERN II were not stopped in the detector to measure the muon polarization; the muon decay in flight was used instead. In the muon rest frame, the energetic electrons fly predominantly parallel (in the case of μ^-, antiparallel) to the muon spin: $\sim (1 \pm A\cos\Theta)$, where Θ is the angle between the muon spin and the electron momentum. More precisely, in the ultrarelativistic limit $m_e \to 0$ (see, e.g., [183]), the angular and energy spectrum of electrons is given by the formula

$$\frac{d\Gamma}{d\varepsilon\, d\Omega} \sim 2\varepsilon^2(3-2\varepsilon)\left[1 \pm A(\varepsilon)\,\cos\Theta\right], \qquad (60)$$

where

$$A(\varepsilon) = \frac{2\varepsilon - 1}{3 - 2\varepsilon},$$

the sign $\pm$ corresponds to the muon charge, and ε is the electron energy divided by its maximum value.

After the transition to the laboratory frame in which the muon moves, the angular anisotropy in the rest frame turns into a dependence of the momentum distribution of the decay electrons on the muon spin. This effect can be explained as follows. We assume that monoenergetic electrons are produced from muon decay in the rest frame. Then the electrons flying along the muon direction have the maximum energy in the laboratory frame. The fraction of such electrons increases if the muon spin is directed along its motion (against for μ^-). If a threshold electron energy is chosen, the number of detected electrons oscillates with the frequency ω_a: it increases when the muon spin is aligned with the muon momentum and decreases to a minimum in the case of counter-alignment (and conversely for μ^-). In fact, the situation is more complicated because the electron spectrum is not monoenergetic, but this does not change the picture qualitatively. By selecting electrons with energies above the threshold in the laboratory frame, we predominantly select the ones moving in a certain direction in the rest frame, and the number of such electrons oscillates together with the muon spin precession.

To detect electrons produced in muon decays, counters were mounted at the inner radius of the storage ring. The momentum of most of the decay electrons is smaller than that of the muon, and therefore they fly inside the storage ring and hit the counters. The detection threshold was set at ~ 750 MeV, which approximately corresponds to a maximum value of NA^2, which, as follows from (59), determines the statistical error in precession frequency measurements.

The relativistic increase in the muon lifetime enabled the experimental measurement of about 20 precession periods (Fig. 19) with an uncertainty of 265 ppm: $a_\mu(\text{CERN II}) = (11661.6 \pm 3.1) \times 10^{-7}$. The measurement uncertainty of a_μ in the CERN II experiment was 15 times higher than in the CERN I experiment. In addition, for the first time, the anomalous magnetic moment of muons of both signs was measured (in all previous experiments, it was measured only for μ^+) and a CPT violation bound was established: $a_{\mu^+} - a_{\mu^-} = (5.0 \pm 7.5) \times 10^{-7}$.

One more feature of the experiment should be noted. For the first time, analysis of muon beam debunching was performed to measure the momentum distribution of captured muons (the bunch structure is well seen in the bottom distribution in Fig. 19). This method has been used in all subsequent experiments.

The magnetic field inhomogeneity needed to keep the muons stored limited the measurement precision: the contribution due to the magnetic field uncertainty to the total measurement error $\delta a_\mu = 3.1 \times 10^{-7}$ was about 1.9×10^{-7}.

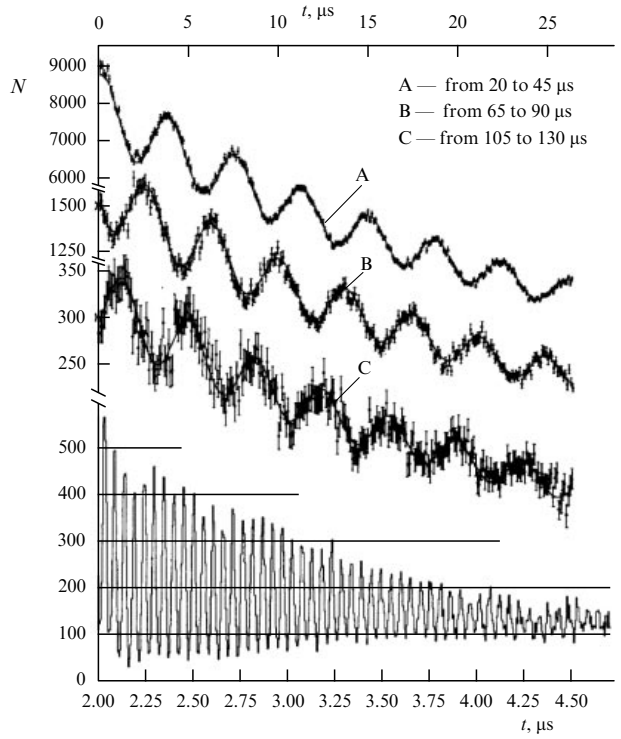

Figure 19. Number N of detected decay electrons as a function of time after injection in the CERN II experiment. Shown is the approximation by function (58) [24].

Any further significant precision increase in the CERN II experiment was virtually impossible.

Meanwhile, there was great interest among the scientific community in improving the measurement accuracy of a_μ. In 1969, when the CERN II result was published, small differences between the theory and experiment, of the order of 2 to 3 standard deviations, were observed for the anomalous magnetic moments of the electron and muon and the Lamb shift (these deviations were later removed due to improvement in the theory) [184]. In addition, it seemed interesting to achieve an accuracy at which the contribution due to strong interactions would be significant (which for the muon is about 60 ppm).

The last of a series of experiments at CERN, CERN III [25, 26], performed in 1969–1976, established the 'gold standard' for subsequent experiments. The setup of the experiment (Fig. 20) was based on that of the CERN II experiment: muons were stored in a special ring with a homogeneous magnetic field, and their polarization was measured by detecting electrons from muon decays (Fig. 21). However, a number of fundamental improvements allowed surpassing the CERN II limitations.

The main contribution to the systematic error was due to the magnetic field gradient needed to keep muons in the vertical direction. In principle, there is no relation between the spin precession and the vertical focusing: the former is determined by the rest-frame magnetic field and the latter by the electric field, and these fields can be formed independently. In the CERN II experiment, the same magnetic field was used for both precession and storage. In the CERN III experiment, a highly uniform magnetic field was achieved, with the electric field formed by a system of eight electrostatic quadrupoles located along the ring. This allowed achieving

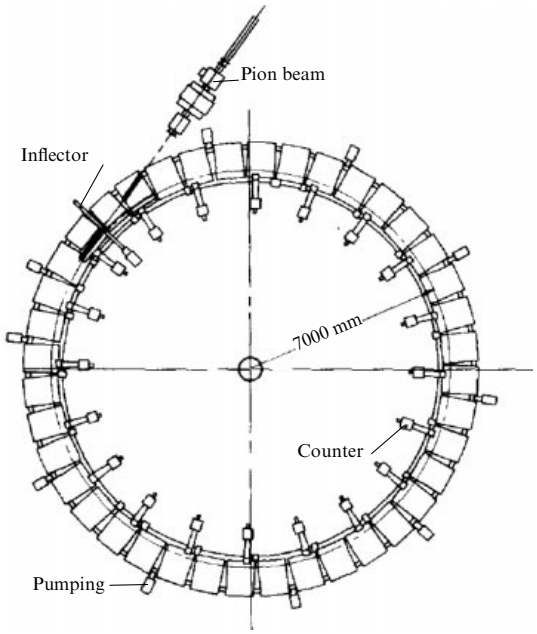

Figure 20. General schematic of the CERN III experiment [25].

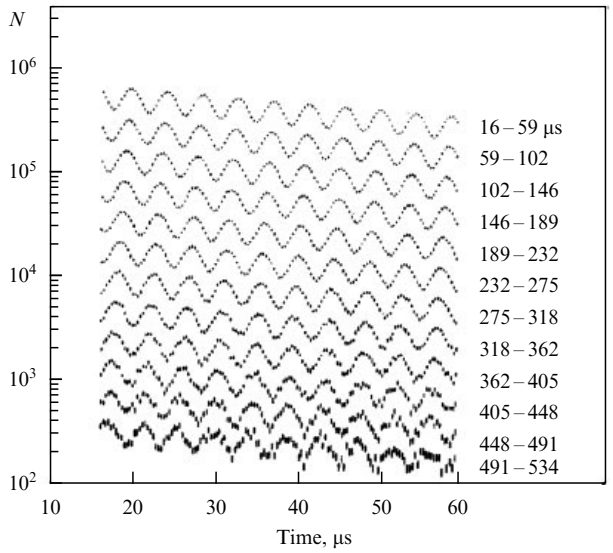

Figure 21. Number N of detected electrons as a function of time after injection [25].

the mean magnetic field uniformity observed by muons (i.e., the field averaged over the ring circumference) of about a few ppm, which is two orders of magnitude better than in the CERN II experiment. Thanks to the high magnetic field uniformity, systematic errors related to the uncertainty in the precise trajectory of muons and muon losses from the beam were reduced dramatically.

However, the electric field affects the muon spin precession frequency; therefore, in general, the uncertainties in the electric field value and the muon orbit trajectory lead to a systematic error in the a_μ measurements. This problem was bypassed by properly choosing the experimental parameters. In the presence of an electric field, the cyclotron frequency is

$$\boldsymbol{\omega}_c = -\frac{e}{m}\left(\frac{\mathbf{B}}{\gamma} - \frac{\gamma}{\gamma^2 - 1}\frac{\boldsymbol{\beta}\times\mathbf{E}}{c}\right), \tag{61}$$

and the spin precession in the rest frame has the form

$$\boldsymbol{\omega}_s = -\frac{e}{m}\left[\left(a_\mu + \frac{1}{\gamma}\right)\mathbf{B} - a_\mu \frac{\gamma}{\gamma+1}(\boldsymbol{\beta}\mathbf{B})\boldsymbol{\beta} - \left(a_\mu + \frac{1}{\gamma+1}\right)\frac{\boldsymbol{\beta}\times\mathbf{E}}{c}\right]. \quad (62)$$

The difference between these frequencies is

$$\boldsymbol{\omega}_a = \boldsymbol{\omega}_s - \boldsymbol{\omega}_c = -\frac{e}{m}\left[a_\mu \mathbf{B} - a_\mu \frac{\gamma}{\gamma+1}(\boldsymbol{\beta}\,\mathbf{B})\boldsymbol{\beta} - \left(a_\mu - \frac{1}{\gamma^2-1}\right)\frac{\boldsymbol{\beta}\times\mathbf{E}}{c}\right]. \quad (63)$$

In the experiment, the muons move perpendicular to the magnetic field, $\boldsymbol{\beta}\,\mathbf{B} = 0$, and hence the final expression for the muon spin precession frequency relative to the momentum has the form

$$\boldsymbol{\omega}_a = -\frac{e}{m}\left[a_\mu \mathbf{B} - \left(a_\mu - \frac{1}{\gamma^2-1}\right)\frac{\boldsymbol{\beta}\times\mathbf{E}}{c}\right]. \quad (64)$$

By choosing muons with such a momentum, when the equality $1/(\gamma^2-1) = a_\mu$ holds, the term related to the electric field vanishes, and we arrive at simple formula (57). The corresponding momentum, which was called the 'magic momentum' in the literature, is $p_{\text{magic}} = 3.094$ GeV/c, $\gamma_{\text{magic}} = 29.3$.

Just this muon momentum was used in the CERN III experiment. This was the key change in the measurement scheme compared to CERN II, enabling a new accuracy level to be achieved. The momentum value determined the size of the ring: for a magnetic field of 1.5 T, the ring radius was 7 m.

The next important change was the use of pion injection. Proton injection in the CERN II experiment, where the proton target was located inside the storage ring, had a number of disadvantages: (1) a low muon capture efficiency, (2) a high background level, and (3) a relatively low initial muon polarization (about 25%) due to a large admixture of muons from high-energy pion decays. In the CERN III experiment, the proton target was placed outside the ring. The optics of the pion channel enabled selecting pions with a momentum of 3.11 GeV/c, which was slightly higher than the 'magic' one, with $\Delta p/p = 0.75\%$. To inject the pion beam into the muon storage ring, a pulsed inflector was used, which for ~ 10 μs compensated the main magnetic field along the pion bunch path. The pions were injected into the ring tangent to the equilibrium orbit at a somewhat larger radius. As in the CERN II experiment, the kick was realized by the pion decay: the muons flew out almost in the forward direction, where they were captured by the storage ring. Only 25% of the pions had time to decay during the first revolution, after which the remaining pions struck the inflector wall. A major advantage of pion injection was the high polarization of the captured muons, about 95%, which was achieved thanks to pion bunch monochromaticity. In addition, the background observed immediately after the injection was drastically reduced.

In the CERN III experiment, the method of beam 'scraping' was used for the first time. During a short time interval after injection, the voltage at the electrostatic quadrupoles was changed, resulting in the muon bunch shift. The particles at the phase space boundary hit the collimator and rapidly escaped from the beam. After resetting the voltage on the electrodes, the 'stripped' beam returned to the standard orbit. This technique enabled a drastic decrease in the number of muons escaping the storage ring during measurement.

As in the CERN II experiment, the muon polarization was measured by detecting electrons produced in muon decays. For this, 20 counters were mounted at the inner ring radius. The use of a large number of counters evenly placed along the ring enabled increasing the detection efficiency of the decay electrons several-fold compared with the CERN II experiment.

In the CERN III experiment, more than 100 spin precession periods were observed (Fig. 21) and a measurement uncertainty of 7.3 ppm was reached: $a_\mu(\text{CERN III}) = (1165923 \pm 8.5) \times 10^{-9}$. The anomalous magnetic moment was measured for muons of both signs, and a new bound on CPT invariance violation was established: $a_{\mu^+} - a_{\mu^-} = (25 \pm 16) \times 10^{-9}$ (10 ppm). The CERN III result confirmed the contribution due to strong interactions to an accuracy of 10%.

The measurement uncertainty of a_μ in the CERN III experiment was improved by a factor of 35 over the CERN II experiment due to a fundamental change in the experimental scheme: the use of muons with the momentum $p_{\text{magic}} = 3.094$ GeV/c. In addition, increasing the muon polarization from 25% to 95% played an important role. The systematic measurement error was estimated to be 1.5 ppm, i.e., the measurement uncertainty was determined by statistics.

In a series of three measurements conducted at CERN, a setup of the 'ideal' experiment to measure the muon anomalous magnetic moment was developed. Many limitations encountered by the CERN III experiment were purely technological. A further increase in accuracy was made possible due to the general technological development without a major revision of the experimental setup.

3.2 E821 experiment at Brookhaven National Laboratory

Around 1984, a collaboration for a new experiment to measure a_μ, E821, was created at the Brookhaven National Laboratory (USA). The preparation for and running of the experiment took almost 20 years. The following fundamental improvements over CERN III enabled achieving a new accuracy level.

(1) The proton beam intensity in the AGS (Alternating Gradient Synchrotron) of BNL was two orders of magnitude higher than in the PS beam (CERN III).

(2) In the E821 experiment, polarized muons were injected into the ring, which significantly (by approximately a factor of 300) increased the muon production efficiency and decreased the background during injection. Muon injection required adding a new element to the storage ring — a muon kicker.

(3) The main magnetic field in E821 was produced by a superconducting magnet enabling a high field stability. A special construction of the magnet provided the field uniformity up to 1 ppm, several times better than in the CERN III experiment.

(4) The electronics of the calorimeters installed to detect decay electrons allowed digitizing the signal shape and the energy deposition in the calorimeters. This made it possible to significantly decrease systematic errors due to the dependence of the detection efficiency on the instantaneous calorimeter load, in particular, due to the overlap of signals from several electrons (pileup).

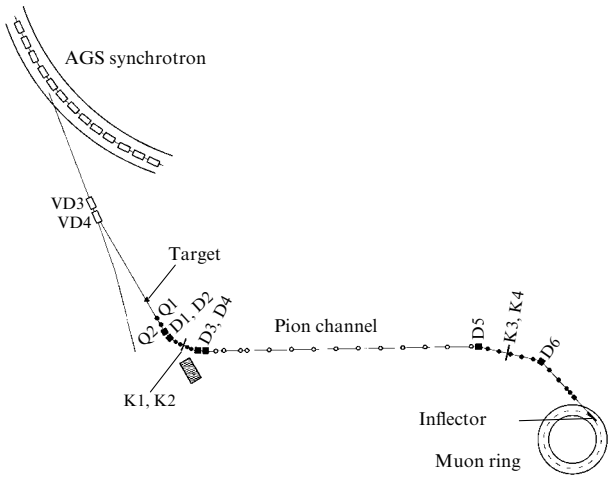

Figure 22. General schematic of the E821 experiment at Brookhaven National Laboratory for measuring the muon anomalous magnetic moment [27].

To produce polarized muons with a momentum of 3.094 GeV/c, a proton bunch with a momentum of 24 GeV/c from the AGS was directed toward a nickel target (Fig. 22). Energetic pions created in the target at a small angle to the direction of the incoming protons were collected and directed into the channel in which turning magnets and the K1, K2 collimator system selected particles with a momentum slightly exceeding the required muon momentum. The selected pions were directed to a decay channel 80 m in length, where a noticeable portion of the pions decayed. The system of turning magnets and the K3, K4 collimators at the output of the channel allowed selecting the particles (muons) with a mean momentum of 3.094 GeV/c.

The parameters of the channel were chosen to optimize the properties of the bunch injected into the storage ring. The key parameters of the experiment included the number of captured muons, the muon polarization, and the number of pions injected together with muons. Using modeling and during the commissioning and running of the channel, an optimal configuration was found in which the K1, K2 collimator selected pions with a momentum of 3.115 GeV/c, $(1.7 \pm 0.5)\%$ higher than the required muon momentum. In such a configuration, approximately 10^{-5} pions per proton reached the rectilinear channel, and 1.2×10^{-7} muons were injected into the storage ring; here, the muon bunch polarization was 95%.

One running cycle of the AGS lasted 2.7 s; during this time, up to 70×10^{12} protons could be stored in the synchrotron. The mean intensity of the AGS proton beam was almost 200 times as high as in the CERN III experiment. The accumulated beam was split into several bunches that were directed onto the target with a period of 33 ms. The number of bunches that was fixed in each experimental run varied from 6 to 12 from run to run. In order to not destroy the target, the intensity of each bunch was limited to 7×10^{12} protons. After passing through the decay channel and momentum selection, the particle beam was an approximately equal mixture of electrons, muons, and pions, as well as of protons, whose number was estimated to be 1/3 that of pions [185].

To inject the particle beam into the storage ring, a superconducting inflector magnet was constructed so as to create a constant uniform magnetic field compensating the main field of the storage ring [186, 187]. A unique feature of the magnet was its ability to not distort the main magnetic field within the measurement errors (fractions of ppm) in the region of the captured muon orbits at a distance of only 3 cm from the injected particle trajectory, where this field was fully compensated. This was made possible by two construction solutions. A uniform field compensating the field of the storage ring was produced by a double cosine coil enabling scattered field compensation. A residual field outside the inflector was compensated by a passive superconducting shield. The field in the principal magnet of the storage ring was powered when the inflector was switched off and the superconducting shield was in the normal state. After completion of the feeding, the inflector shield was turned into the superconducting state, thus 'freezing' the field inside the inflector. After that, the field was introduced into the inflector.

During three experimental runs (1997–1999), the superconducting inflector shield was damaged (after opening it to repair the inflector), which resulted in the appearance of scattered fields of the order of 600 ppm. However, because the field nonuniformity was localized and only the field integral over the entire storage ring was important, the additional contribution to the systematic error was less than 0.2 ppm. In addition, the integral of the statistics collected over these three operational periods was around 10% of the total integral, and this additional contribution did not strongly affect the systematic error of the final result. After the end of the 1999 run, a new inflector with an undamaged shield was installed, which fully solved the problem of the scattered inflector field.

In the uniform magnetic field of the storage ring, the injected beam moves in a circular orbit; therefore, after one revolution (149 ns), it would strike the inflector wall. For the beam to be in the equilibrium orbit, it must be 'kicked' during the first revolution. To do this, at 1/4 of the revolution from the inflector, a kicker [188] was mounted, which, during a short time interval with a duration about one beam revolution, produced an integral of the field ~ 0.1 T m, corresponding to a beam turn through about 10 mrad. The magnetic field was generated by a short pulse (about 400 ns) of the current formed by an LRC chain. The current flows along two aluminum parallel plates 1.76 m in length (placed to the right and to the left of the muon storage region), forming one coil. To produce the necessary field integral, three consecutive identical kickers were installed (K1–K3 in Fig. 23).

In the E821 experiment, electrostatic focusing was used, as proposed in the CERN III experiment. A quadrupole electric field was formed by four groups of electrodes [189] symmetrically located along the ring (Q1–Q4 in Fig. 23). For technological reasons, it was impossible to place the electrodes along the entire ring without gaps: in the E821 ring, the electrodes fill 43% of its perimeter. However, such a filling and four-fold symmetry was sufficient to form almost the same beam size along the perimeter: the ratio of the maximum to minimum beam size is $\sqrt{\beta_{\max}/\beta_{\min}} = 1.04$. Because the acceptance of the detectors depends on the beam size, such a uniformity is crucial for decreasing systematic errors in the ω_a measurements.

In the typical operation mode, before the injections, the electrodes were fed by a voltage of about 25 keV, which was sustained during the entire measurement cycle, 700 μs – 1 ms. Immediately before the injection, different voltage was

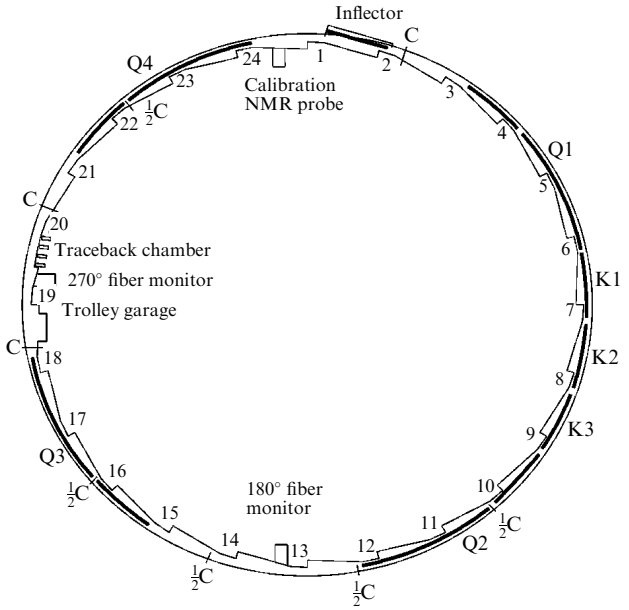

Figure 23. Storage ring layout. K — kickers, Q — electrostatic quadrupoles, C — collimators. Numbers on the inner ring show the location of calorimeters.

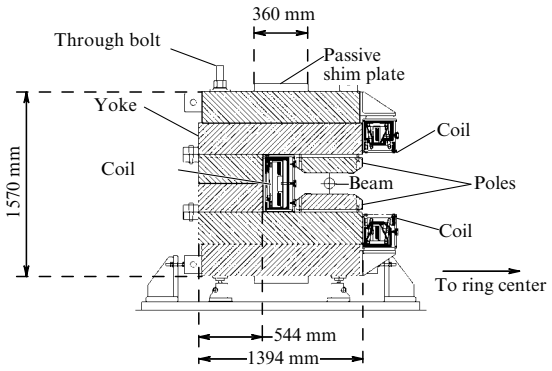

Figure 24. Cross-section view of the storage ring [27].

supplied to the electrodes, which shifted the equilibrium orbit by several millimeters. The shifted beam was scraped using a system of collimators mounted along the ring perimeter (ring C collimators and semiring 1/2 C collimators in Fig. 23). In 7 to 16 μs, the electrode voltage was symmetrized and the beam returned to the standard equilibrium orbit. This procedure made it possible to decrease the phase space population near the boundary, which enabled a decrease in the number of muons escaping the beam and not decaying before that. Such muons can cause a systematic error because the spin direction of the lost muons cannot be measured.

The described scheme of generation and storage of the muon beam enabled capturing approximately 10^4 muons per proton bunch ($\sim 5 \times 10^{12}$ p), which is two orders of magnitude larger than in the CERN III experiment.

To achieve a high measurement accuracy of the muon anomalous magnetic moment, a highly uniform magnetic field must be generated in the muon storage region. Formula (57) contains the mean magnetic field 'observed' by a muon. To provide the required measurement precision, the mean magnetic field should be measured with an absolute uncertainty of the order of 0.1 ppm. In addition, because the orbits of individual muons are different, the mean magnetic field should be made uniform across the entire storage region for spins of muons captured in different equilibrium orbits to precess synchronously. The admissible vertical and radial magnetic field variation averaged over the perimeter is about 1 ppm. Much larger local nonuniformities, up to 100 ppm, are allowed if they remain stable in time and can be measured with an uncertainty that does not damage the mean field determination uncertainty.

The storage ring is a solid magnet [190] enabling a high field uniformity in the storage region. A schematic of the magnet is shown in Fig. 24. The magnetic field is created by four 14 m 24-coil superconducting coils. At the time of manufacturing in 1996, these were the world largest superconducting coils. Two coils mounted on one shell were put in a cryostat at the outer radius of the muon beam. Two other coils, each in an individual cryostat, were located at the inner radius. The coils were fed by an external stabilized current source with a nominal current of 5200 A. The feedback loop with the magnetic field measurements by nuclear magnetic resonance (NMR) probes allowed the field stability at a level of several ppm to be achieved. The magnetic field configuration was determined by a C-like yoke made of standard low-carbon steel AISI 1006 (AISI: American Iron and Steel Institute). The field in the muon storage region is formed by special poles made of a vacuum-processed steel with very low carbon content (less than 4 ppm). The technology of production of such a steel ensures a low number of local defects and bubbles, which is very important for producing a uniform magnetic field. The magnet yoke consists of 36 individual elements (six sectors with six elements each) precisely adjusted to each other and electrically insulated. The magnetic poles include 24 elements: 12 sectors each with top and bottom poles.

The magnet design included a set of elements for passive shimming and a system of coils for active shimming of the magnetic field, which were placed on the surfaces of the poles. Several successive approximations were required to achieve the required field uniformity. The initial magnet shimming was performed before the first run (1997), and the field was uniform at the level of about 25 ppm. The uniformity was significantly improved already by the next run (1998). Ultimately, a uniformity of ± 1 ppm was achieved after replacing the superconducting inflector before the 2000 run, and about 90% of the experimental statistics were taken with this field configuration. Figure 25 shows the magnetic field map in the 2001 run.

The magnetic field in the storage ring was measured and monitored by the NMR method [191] in units of the free proton precession frequency ω_p. Continuous field measurement with the required accuracy in the large storage ring volume required the use of a multi-step sensor system.

To determine the absolute value of the field, a special NMR probe [192] filled with a highly pure water was used. The NMR method does not allow the direct measurement of free proton precession because the proton magnetic moment is screened by the sample medium. However, the construction of the device and the sample medium have been chosen so as to enable the measurement of ω_p by measuring the precession frequency in water. The total correction, which is quite large, approximately 25.8 ppm, is determined by the diamagnetic screening of a proton in a water molecule. The value of the correction is known to an accuracy of 14 ppb, which is much

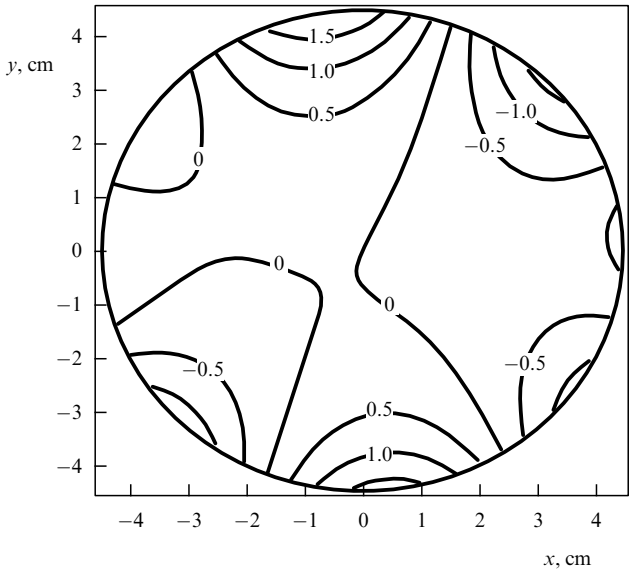

Figure 25. Two-dimensional map of the magnetic field averaged along the storage ring circumference in the muon storage region (2001 run data).

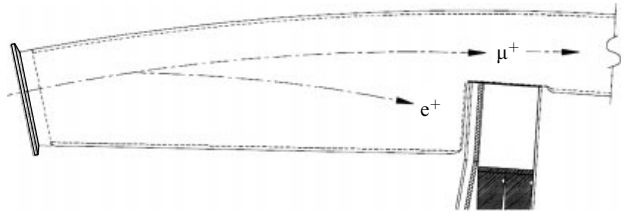

Figure 26. Calorimeter (bottom right) installed on a special step in the vacuum chamber [194].

Table 3. Systematic uncertainty (in ppm) of measurements of the magnetic field ω_p in the storage ring.

Systematic error source	1999	2000	2001
Absolute calibration of standard probe	0.05	0.05	0.05
Calibration of trolley probes	0.20	0.15	0.09
Magnetic field measurement	0.10	0.10	0.05
Interpolation with fixed probes	0.15	0.10	0.07
Uncertainty from space muon distribution	0.12	0.03	0.03
Inflector fringe field uncertainty	0.20	—	—
Others	0.15	0.10	0.10
Total systematic error in ω_p	0.4	0.24	0.17

better than the experimental requirement for the magnetic field measurement uncertainty. Recent new measurements of diamagnetic screening in water [193] with an uncertainty of 2.5 ppb are fully consistent with the previous value taken to calculate ω_p. With all effects taken into account, the magnetic field measurement uncertainty using the absolute calibration probe is estimated to be 0.05 ppm.

To map the field in the entire muon storage volume, a special trolley was used, on which 17 NMR probes were mounted. Using a line and wire, the trolley could move on special rails inside the vacuum chamber along the entire circumference of the storage ring. During the accumulation of statistics, the trolley was parked in a special 'garage' (see Fig. 23). During the experimental run, the field was mapped 2–3 times a week for about 2 hours.

The field was continuously monitored both during the data taking periods and between them using a system of 378 'stationary' NMR probes of the same type as those mounted on the trolley. The stationary probes were mounted on the top and bottom walls of the vacuum chamber at two or three radial positions every 5 degrees along the ring circumference. The mean magnetic field measured by a subset of 36 stationary probes evenly distributed along the circumference was used in a feedback loop to sustain a constant field in the storage ring magnet.

The main contributions to the systematic measurement error of ω_p are listed in Table 3 for three runs during which the main integral of statistics was collected. During that time, the total systematic error was decreased by a factor of two due to numerous improvements in the experiment.

Electrons and positrons that were products of muon decays were detected by 24 electromagnetic calorimeters [194] evenly located near the vacuum chamber at the inner storage ring radius (locations of the calorimeters are shown in Fig. 23). To minimize the amount of matter in front of the calorimeter, the storage vacuum chamber was specially shaped, as shown in Fig. 26. Each calorimeter included a grid of scintillating fibers 1 mm in diameter mounted into a lead alloy matrix (glued into grooves etched out in a lead alloy plate). The scintillating fibers were directed along the storage ring radius (such that an electron entered the calorimeter perpendicular to the fiber direction). Four photomultipliers (PMTs) were used for the readout. For electrons with an energy of 1.8 GeV (the threshold energy for ω_a measurements), the time resolution was about 100 ps with an energy resolution of about 7 %.

Measuring ω_a requires neither a high time resolution nor a high energy resolution. At the same time, it is extremely important that the resolution and the mean calorimeter response are independent of the instant calorimeter load. To calibrate the calorimeter response stability, a special laser calibration system was designed. The calibration showed that under a high calorimeter load, the systematic shift of the reconstructed time of the signal does not exceed 4 ps. The dependence of the energy calibration of the calorimeter on the load does not exceed a few fractions of one percent, which was compensated in the data analysis.

To estimate different systematic effects and carry out auxiliary measurements, additional detectors mounted together with calorimeters were used. On the front plane, about half of the calorimeters were supplied with front scintillating detectors (FSDs) 1 cm in thickness (Fig. 27). They were used to measure the vertical distribution of the electron entry point into the calorimeter, which was then used to estimate some systematic effects and to measure the muon electric dipole moment. Moreover, FSDs allowed studying the effects related to the loss of muons from the storage ring: the low detection threshold of the FSDs enabled such muons to be detected by coincidence of signals from several stations.

In front of one of the calorimeters (number 20 in Fig. 23), a hodoscope was placed consisting of four chambers, each containing three layers of horizontal and vertical drift tubes 8 mm in diameter. This system was used to measure the muon decay point. For this, the reconstructed track of an electron that escaped from the ring and entered the calorimeter was traced backwards (hence the name, traceback system). These measurements were used to study the muon beam dynamics in the storage ring when measuring the muon EDM.

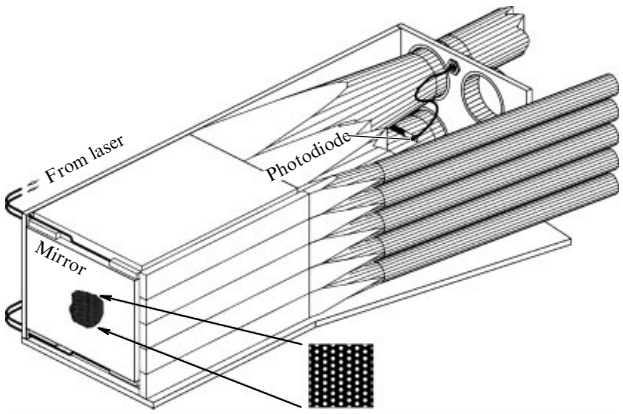

Figure 27. Schematic view of the calorimeter [27].

Analogue signals from four PMTs watching one calorimeter were summed and directed into two channels of four-channel waveform digitizers (WFDs), which continuously digitized the incoming signals with a frequency of 200 MHz and an 8-bit resolution. The reference generators of a pair of channels digitizing the signal from one calorimeter were half-period shifted, which enabled the effective doubling of the digitizing frequency to 400 MHz. To decrease the data volume, the zero suppression was used: when the discriminator threshold was exceeded, the signal shape from the corresponding channel with a duration of 80 ns was stored in the buffer memory, with 16 ns being the time before the discriminator was triggered to measure the baseline.

Figure 28 shows the structure of the data formed in WFDs for each muon injection into the storage ring. Approximately 50 μs before the injection, the control system of the AGS synchrotron issued a triggering signal for the operation mode of the experimental data readout. First, the calorimeter PMTs were gated off by redistributing the dynode high voltage. The decrease in the amplification coefficient by a factor of $\sim 10^6$ made it possible to avoid long-term effects caused by the PMT signal saturation during the injection. Then the electronics of the data acquisition system formed a triangle-like signal that was used to synchronize WFD plates. Several microseconds after the injection, the PMT dynodes were supplied by a standard voltage, and the WFDs started digitizing the data. The digitizing continued 700–1000 μs after the injection, and data were stored in the WFD buffer memory, from where they were taken by the data acquisition system during the pause between injections.

A large number of neutrons created during the injection produced a continuous background signal (a pedestal) evolving as $\sim t^{-1.3}$. As long as the pedestal was above the threshold, the WFDs worked, in fact, in the continuous digitizing regime. When the pedestal fell below the threshold, the WFDs collected only the pulses above the threshold. The pedestal level varied significantly in different detectors. The maximum pedestal was observed in detectors located along the injected beam path (especially in detectors *3–6*). In these detectors, a maximum time delay of about 27 μs between the injection and the turn-on of PMTs was set in order to decrease the PMT illumination effect and to shorten the continuous digitization time interval to an acceptable level, avoiding the overload of buffers. The minimum pedestal level was observed in detectors located against the beam propagation direction relative to the inflector. In these detectors, PMTs were powered almost immediately after the injection with a time delay of 2–5 μs.

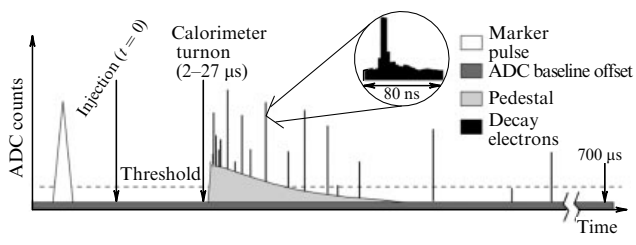

Figure 28. Record corresponding to one injection into the storage ring.

In measurements of ω_a, the resolutions of energy and time measurements are not very significant; however, the measurement stability during the time interval from the beginning of injection to the end of digitizing (about 1 ms) is very important. Because the calorimeter load is about a few megahertz immediately after the injection and decreases by several orders of magnitude in 1 ms, the stability requirement means that the reconstruction results must not depend systematically on the instantaneous load. The most important parameter from the standpoint of measurements of ω_a is the reconstructed electron arrival time. To ensure a systematic error less than 0.1 ppm in the ω_a measurement, the stability of the reconstructed time inside the digitizing interval (1 ms) must be better than 20 ps, which is two orders of magnitude shorter than the signal sampling time.

One of the principal effects leading to the dependence of the reconstruction results on the load is related to signal overlapping (pileup). For a typical calorimeter load, immediately after the injection, with a probability of a few percent, two or more electrons enter the calorimeter within a short time span, such that their signals overlap. This probability decreases to almost zero by the end of the digitizing interval.

The method to reconstruct the events was based on the approximation of the measured shape of the signal by a standard shape (or the sum of standard signals in the case of pileup). The standard signal shapes were determined for each calorimeter from the data. For this, single electron signals detected 300 μs or later after the injection were used. The fraction of events including two or more overlapping electron signals decreased by that time by more than two orders of magnitude, to become negligibly small. For each experimental run, an independent calibration of the mean signal shape was performed. Dedicated studies were carried out to monitor the signal shape stability over the run, as well as the dependence of the signal shape on its time of arrival relative to the injection time.

The energy calibration of the calorimeters was done using the edge electrons corresponding to approximately 3.1 GeV. A precise absolute energy calibration is not required to measure ω_a; however, it is very important that the calibration remain stable within the digitalization interval. To establish the degree of calibration stability, the dependence of the mean energy release of electrons with energies above the threshold on the signal arrival time after the injection was measured; here, a correction for the pileup was made. For each calorimeter, the function of the energy scale change with time, $\Delta G/G(t)$, was determined and used as a correction in the data analysis. For most of the calorimeters, the value of $\Delta G/G$ did not exceed 0.2% several microseconds after injection.

To measure the spin precession frequency, the time distribution $N(t)$ of electrons with energies (measured by calorimeters) above a certain threshold is constructed. In the ideal case, the distribution can be described by the function

$$N(t) = \frac{N_0}{\gamma\tau_\mu}\exp\left(-\frac{t}{\gamma\tau_\mu}\right)\left[1 - A\cos\left(\omega_a t + \phi\right)\right], \qquad (65)$$

where the distribution parameters N_0, A, and ϕ depend on the electron threshold energy. The calculated spectrum $N(E)$ and asymmetry $A(E)$ for decay electrons in the experimental conditions are presented in Fig. 29. The statistical error of the ω_a determination is proportional to NA^2. When electrons with an above-threshold energy are used to determine ω_a, the electron threshold energy value that minimizes the statistical error is 1.8 GeV.

Figure 30 shows the distribution $N(t)$ for electrons with energies above 1.8 GeV for one run (2001). In the first approximation, to determine the precession frequency, this distribution is approximated by formula (65) with five free parameters (N_0, τ_μ, A, ω_a, and ϕ). In the analysis of data collected in 1998 (about 1% of the total experimental statistics), this function was sufficient to describe the experimental data: the value of the reduced χ^2/v (where v is the number of degrees of freedom) was close to unity. However, with increasing the statistics, the fitting function

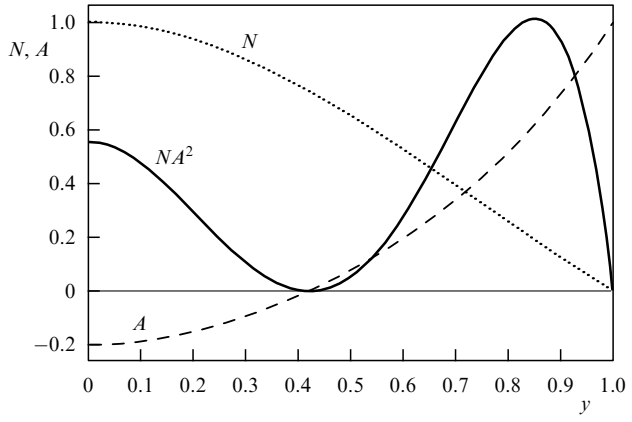

Figure 29. Calculated electron spectrum and asymmetry in the laboratory frame. Shown is the energy fraction $y = E_e/E_{max}$.

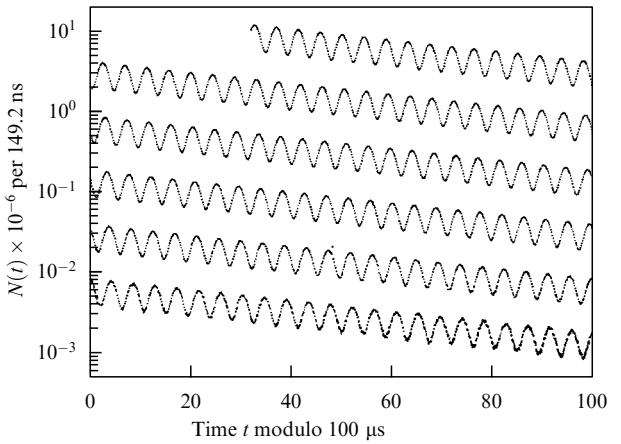

Figure 30. Time distribution $N(t)$ for electrons with the energy above 1.8 GeV for data taken in 2001 [27].

should take a number of additional effects into account. The complete fitting function to approximate the distribution $N(t)$ that takes all known effects into account has the form

$$N(t) = \frac{N_0}{\gamma\tau_\mu}\exp\left(-\frac{t}{\gamma\tau_\mu}\right) A(t)\, V(t)\, B(t)\, C(t)\times \\ \times\left\{1 - A(t)\,\cos\left[\omega_a t + \phi(t)\right]\right\}, \qquad (66)$$

where

$$A(t) = 1 - A_{loss}\int_0^t L(t')\exp\left(-\frac{t'}{\gamma\tau_\mu}\right)\mathrm{d}t', \qquad (67)$$

$$V(t) = 1 - \exp\left(-\frac{t}{\tau_{VW}}\right) A_{VW}\cos\left(\omega_{VW}t + \phi_{VW}\right), \qquad (68)$$

$$B(t) = 1 - A_{BR}\exp\left(-\frac{t}{\tau_{BR}}\right), \qquad (69)$$

$$C(t) = 1 - \exp\left(-\frac{t}{\tau_{CBO}}\right) A_1\cos\left(\omega_{CBO}t + \phi_1\right), \qquad (70)$$

$$A(t) = A\left[1 - \exp\left(-\frac{t}{\tau_{CBO}}\right) A_2\cos\left(\omega_{CBO}t + \phi_2\right)\right], \qquad (71)$$

$$\phi(t) = \phi_0 + \exp\left(-\frac{t}{\tau_{CBO}}\right) A_3\cos\left(\omega_{CBO}t + \phi_3\right). \qquad (72)$$

Correction functions (67)–(72) and their parameters are discussed below. These additional effects must be taken into account to obtain a good value of χ^2/v for the fit; however, most of the additional factors rather weakly affect the determination of ω_a.

With decreasing the threshold energy below 1.8 GeV, the number of events in the $N(t)$ distribution increases, but the statistical accuracy of ω_a worsens. This is because events with low anisotropy (or even with the opposite sign) are added to the histogram, which decreases the mean asymmetry. However, if ω_a is measured independently in different electron energy intervals, it is possible to avoid asymmetry 'smearing' and to optimally use all information about ω_a that is carried by electrons with different energies. A similar result can be obtained if electrons are assigned the weight $A(E)$ in the distribution $N(t)$. Such an approach is equivalent to the data analysis within infinitely narrow energy bins. This method was used for data analysis in the 2000 and 2001 runs.

An alternative method to determine ω_a is to approximate the ratio

$$r(t) = \frac{n_1(t + T/2) + n_2(t - T/2) - n_3(t) - n_4(t)}{n_1(t + T/2) + n_2(t - T/2) + n_3(t) + n_4(t)}, \qquad (73)$$

where $n_{1,2,3,4}(t)$ are four equal statistically independent subsets of electrons (with $N(t) = n_1(t) + n_2(t) + n_3(t) + n_4(t)$) and T is the precession period ($T \approx 4.37$ μs). The contributions due to 'slow' effects (for example, muon decays) in formula (73) cancel, and therefore in the first approximation $r(t)$ can be described by the function

$$r(t) = A\cos\left(\omega_a t + \phi\right) + \frac{1}{16}\left(\frac{T}{\gamma\tau_\mu}\right)^2 \qquad (74)$$

with three free parameters: A, ω_a, and ϕ. Function (74) is sufficient to describe the ratio $r(t)$ averaged over all detectors; however, for an independent analysis of $r(t)$ for individual calorimeters, a more complicated functional form must be used that takes effects related to coherent betatron oscillations (CBOs) into account: the contributions similar to $C(t)$, $A(t)$, and $\phi(t)$ in Eqn (66). Nevertheless, other contributions due to the 'slow' effects cancel and can be ignored in the analysis. A data analysis based on the approximation of the ratio $r(t)$ was carried out for all runs.

In all cases, the least-square method was used for the approximation, and the value of χ^2/v was used to control the fitting quality. In the typical analysis, the approximation of $N(t)$ or $r(t)$ was made in the time interval from 30 to 630 μs after injection in 149.2 ns bins, i.e., for 4000 points. Correspondingly, the approximation was considered acceptable if χ^2/v fell within the range of 1 ± 0.022. Only bins with at least 30 events were fitted.

At the injection, the muon beam had an approximately Gaussian shape with a width of about 25 ns. The time of one revolution in the ring is about 149.2 ns, which is much longer than the bunch duration, and therefore the beam structure is well recognized in the distribution of the arrival times of electrons in the calorimeter: the $N(t)$ distribution is modulated by a rapidly oscillating function with the period $T_c = 2\pi/\omega_c \approx 149.2$ ns. Due to pulse dispersion $\Delta p/p \sim 10^{-3}$, the injected beam is gradually debunched with the characteristic time of 20 μs. Immediately after the injection, the beam fills 60° of the circumference; the beam front takes over its tail in approximately 5 μs. For most of the detectors, the analysis of $N(t)$ starts 30 μs after the injections. By this time, the bunch structure of the beam is still well observed in the distribution.

To exclude the cyclotron frequency from the distribution $N(t)$, the reconstructed time of detection of electrons was shifted randomly within the interval $(-T_c/2, T_c/2)$. This procedure decreased the visible amplitude of cyclotron oscillations by a factor of 500, which was sufficient for the subsequent analysis.

The analysis of the debunching allows obtaining important information: the spatial distribution of the muons in the radial direction or, closely related to it, the momentum distribution of the muons. A numerical model for beam debunching was constructed, enabling a good description of the observed decay of the cyclotron oscillations in $N(t)$. These results were confirmed by an alternative method based on the Fourier analysis of $N(t)$. The radial muon distribution is important for calculating the mean magnetic field for the entire muon ensemble.

Signal overlapping in the calorimeter significantly distorts the distribution $N(t)$. When two low-energy electrons enter the calorimeter almost simultaneously, they can be detected as one high-energy electron. The phase ω_a of the low-energy electron oscillations differs from that of high-energy electrons; therefore, as regards determining ω_a, the 'electron' from a pileup is significantly different from a true electron with the same energy. Because the pileup fraction decreases with decreasing the calorimeter load, this leads to a systematic phase shift of the phase of ω_a oscillations and hence to a systematic error in the frequency measurements. Under typical experimental conditions, the fraction of 'erroneous' electrons immediately after the injection is about 1% of the total number of electrons with the energy above 1.8 GeV.

To compensate for the pileup effect, additional terms could be added to (66). However, this leads to a significant increase in both statistical and systematic errors of frequency determination. The capability of the read-out electronics to store the signal shape enabled using a much more reliable method of pile-up correction based on the direct measurement of the effect and its subtraction from the $N(t)$ histogram. The method involves a statistical modeling of the pileup contribution. At the 'tail' of each reconstructed signal, a secondary signal was sought in a fixed time interval with a width corresponding to the time resolution of the reconstruction algorithm. If the secondary signal was found, the common signal was formed as if the secondary signal appeared in the calorimeter together with the primary one. Next, the time distribution of the pileups was constructed in which the artificially formed total signal was added with the weight $+1$ and both original signals, primary and secondary, were added with the weight -1, and the resulting distribution was subtracted from the main distribution $N(t)$.

The result of the described procedure is shown in Fig. 31. The pileup contribution is clearly seen in the electron energy spectrum $N(E)$, in which a high-energy 'tail' appears. The pileup energy distribution $P(E)$ is negative in the low-energy range and positive in the high-energy range, corresponding to the fact that two low-energy electrons are missing and one high-energy electron emerges due to the pileup. It is seen that the above procedure allowed a full compensation of the pileup effect.

Due to the presence of the electrostatic quadrupoles, the storage ring of the experiment has a weak focusing with the field index

$$n = \frac{R_0}{\beta B_0}\frac{\partial E_y}{\partial y}\,, \tag{75}$$

where R_0 is the equilibrium orbit radius, B_0 is the main magnetic field magnitude, β is the muon velocity, and $\partial E_y/\partial y$ is the mean gradient of the electric field, taking into account that the quadrupoles cover 45% of the ring circumference. The electrons in such a ring make vertical and horizontal betatron oscillations with the respective dimensionless frequencies $\nu_y = \sqrt{n}$ and $\nu_x = \sqrt{1-n}$. The value of n is determined by the voltage on the quadrupoles, which varied in different experimental runs. In early runs

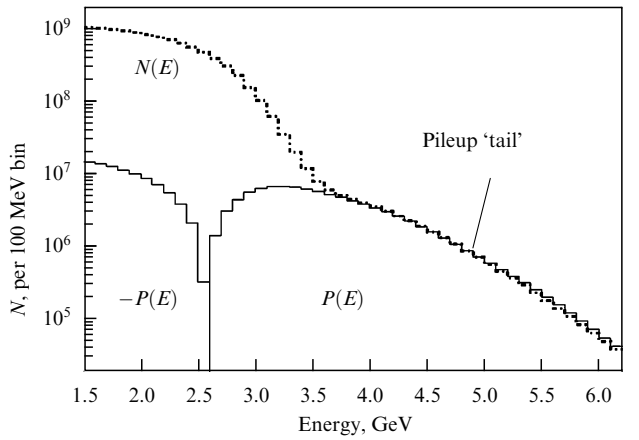

Figure 31. Result of statistical subtraction of the pileup contributions. Shown are the uncorrected energy spectrum of electrons $N(E)$ and the pileup energy spectrum $P(E)$ [27].

prior to and including 1999, data were obtained with $n = 0.137$ (which corresponded to the voltage of ± 24 kV). In the 2000 run, $n = 0.135$ was used. In 2001, the data were taken for two values of n, 0.122 and 0.142.

The inflector aperture (18 mm) is significantly smaller than that of the storage ring (90 mm); therefore, after the injection, the beam fills a rather small part of the phase space of the ring. Due to the angular dispersion in the bunch, its size starts increasing after the injection. However, because the betatron frequency is the same for all muons, in every half-period the bunch is focused again, repeating the infector image. A similar effect occurs because the kicker pulse is not ideal, and after the kick, the bunch moves some distance away from the equilibrium orbit. Synchronous (coherent) betatron oscillations of individual muons result in the entire bunch oscillating around the equilibrium orbit. In the reference frame of an individual calorimeter, beating between these oscillations and the revolution frequency of the beam is observed: the passing beam 'breathes' (its width changes) with frequencies $\omega_c(1 - 2v_x)$ and $\omega_c(1 - 2v_y)$ and oscillates with frequencies $\omega_c(1 - v_x)$ and $\omega_c(1 - v_y)$ in the respective horizontal and vertical directions.

The most significant observable effects turn out to be the coherent horizontal betatron oscillations with the frequency $\omega_{CBO} = \omega_c(1 - \sqrt{1 - n})$ and periodic changes in the beam vertical waist (VW) with the frequency $\omega_{VW} = \omega_c(1 - 2\sqrt{n})$; other oscillations are negligible. The nonideality of the quadrupole electric field and the corresponding dispersion in the field index result in a slow decoherence of the oscillations, which is described quite well by an exponent with a time constant of 100–150 μs and 25 μs for respective horizontal and vertical oscillations. Direct observations of all types of oscillations were performed using fiber beam monitors (FBMs) during special runs with the monitors inserted into the storage region.

The coherent betatron oscillations distort the electron spectrum $N(t)$ via two main mechanisms. The calorimeter acceptance depends on the location of the muon decay point: for example, the proportion of decay electrons detected by the calorimeter is different for muons decaying at different radii. This leads to a modulation of the number of detected electrons and an asymmetry of the ω_a oscillations. The flight time of the electron from the muon decay point of (at which the ω_a-oscillation phase is fixed) to the calorimeter also depends on the radial (horizontal) location of the decay point, resulting in the modulation of the observed ω_a-oscillation phase. When adding data from all calorimeters, $N(t)$ distortions due to coherent betatron oscillations decrease by an order of magnitude.

To observe the $N(t)$ distortions caused by coherent betatron oscillations, a Fourier analysis of the difference between the experimental distribution and its approximation by the simple model in (65) was performed. The obtained frequency spectrum for the 2000 data subset is shown in Fig. 32. Frequencies of the horizontal (CBO) and vertical (VO) coherent betatron oscillations and the vertical waist (VW) frequency of the beam are clearly seen. In addition, beatings between these frequencies and the precession frequency f_a are well observed. The peak at zero frequency corresponds to 'slow' distortions of $N(t)$ due to particle losses from the beam and the residual dependence of the energy calibration on time.

To take effects related to the coherent betatron oscillations into account, model (66) describing $N(t)$ was supplemented with the corresponding terms, in Eqns (68) and (70)–(72), describing the modulation of N due to vertical waist oscillations of the beam and the modulation of N, A, and ϕ caused by horizontal beam oscillations. The modulation parameters were used as free parameters for the approximation of $N(t)$: the decay time of horizontal and vertical oscillations τ_{CBO} and τ_{VW}, oscillation frequencies ω_{CBO} and ω_{VW}, and phases and amplitudes of the modulations A and ϕ. The contribution due to the vertical waist oscillations of the beam is important only when the approximation of $N(t)$ starts at $t < 30$ μs.

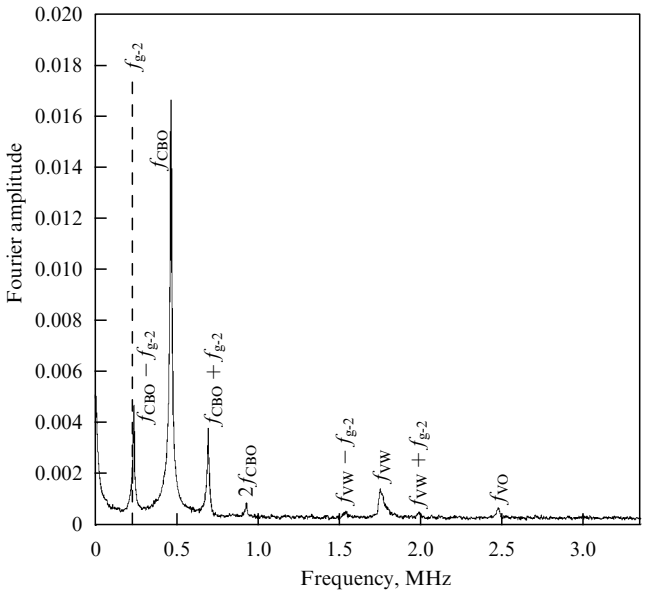

Figure 32. Frequency spectrum obtained from the Fourier analysis of the residuals between the experimental distribution $N(t)$ and its fitting by the simple model (65) (2000 run data). Shown are coherent betatron oscillations (CBO) and the vertical oscillations (VO), the beam waist vertical oscillations (VW), and beat frequency between them and the precession frequency $f_{g\text{-}2} = \omega_a/(2\pi)$ [27].

In the 1998 data analysis, the described effects were not discovered, being much smaller than the measurement statistical errors. In addition, in the 1998 data analysis, the distribution $N(t)$ summed over all calorimeters was used. In the 1999 data analysis, the modulation was experimentally detected first in the form of a periodic dependence of ω_a measured with a single calorimeter data at the location of that calorimeter, and then in a Fourier analysis of $N(t) - N^{5par}(t)$. At the 1999 statistics level, to compensate for this effect, it was sufficient to take modulation into account in the detected number of electrons (70).

The CBO modulation of $N(t)$ was discovered and studied already after the 2000 run had been completed. It turned out that in the 2000 run data, the ω_{CBO} frequency was very close to the double precession frequency [the $f_{CBO} - f_a$ frequency is very close to f_a (see Fig. 32)]. In this case, the result of measurements of ω_a is very sensitive to the correctness of the modulation description. Figure 33 shows the dependence on the frequency f_{CBO} of the relative shift of ω_a from the true value when the modulation is not taken into account in the fitting function. In the 2000 run, the data were taken for different values of n; however, most of the data were collected under the worst conditions. The modulation-related effects were fully explored by the beginning of the 2001 run, and to decrease the corresponding contribution to the systematic

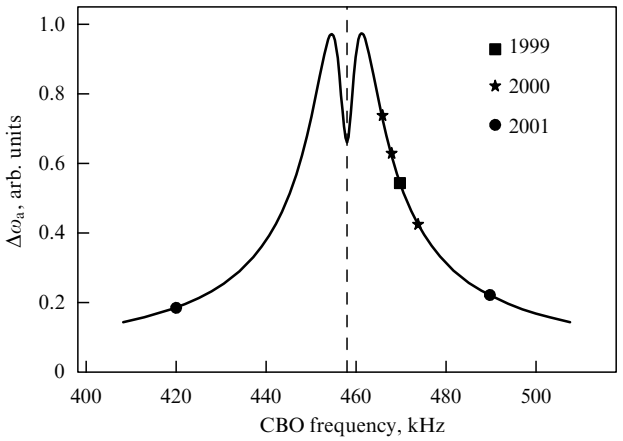

Figure 33. Systematic shift ω_a due to betatron oscillations as a function of the frequency f_{CBO} when the modulation of $N(t)$ is not addressed by the fitting function. Shown are the f_{CBO} frequencies for different experimental runs.

error, the data were intentionally collected in that season for two different values of n such that the frequency $f_{CBO} - f_a$ is far from f_a.

Under the resonance conditions, electric and magnetic field nonuniformities in the storage ring can enhance betatron oscillations, leading to the direct (not induced by muon decays) escape of muons from the storage region. To decrease the losses, the accumulated beam is 'stripped' during the measurements, immediately after the injection. Nevertheless, a small number of muons do escape from the beam during the measurement, with their fraction changing in time. To determine the dependence of the number of lost muons on time $L(t)$, the data obtained with front scintillating detectors (FSDs) mounted before the calorimeter were used. The instant muon loss rate $L(t) \equiv dN_{loss}/dt$ allows determining correction (67) to $N(t)$ due to the muon escape. Because it was impossible to measure the detection efficiency of the lost muons with good accuracy (modeling showed that it was about several percent), function (67) was added with a free normalization parameter A_{loss}. The effects related to the beam relaxation (BR) are taken into account after the 'scraping' procedure is completed by using the correction function $B(t)$ determined by formula (69).

To obtain the final result, the value of ω_a derived using the $N(t)$ approximation should be supplemented with two corrections.

The first is due to vertical betatron oscillations of particles in the stored beam. Due to the oscillations, the direction of the muon momenta is not strictly perpendicular to the magnetic field direction, $\boldsymbol{\beta}\,\mathbf{B} \neq 0$. This results in a small decrease in the precession frequency because of the term proportional to $\boldsymbol{\beta}\,\mathbf{B}$ in (64). This effect was first estimated in [195]. The amplitude of the correction is proportional to the beam waist:

$$\frac{\Delta\omega_a}{\omega_a} = -\frac{\langle\psi_0^2\rangle}{4} = -\frac{n\langle y^2\rangle}{4R_0^2}\,.$$

For the E821 experiment, the beam waist was derived both from simulations [196] and from the traceback system. The amplitude of the correction varied in different runs; for example, in 2001, the correction was -0.270 ± 0.036 ppm.

The second correction is related to the energy dispersion in the beam. For particles with the momentum somewhat different from the 'magic' value, the nonzero factor $a_\mu - 1/(\gamma^2 - 1)$ somewhat decreases the precession frequency in the presence of the electric field [the term proportional to $\boldsymbol{\beta} \times \mathbf{E}$ in (64)]. The frequency shift is proportional to both the momentum dispersion and the electric field amplitude. Both these quantities are directly proportional to the horizontal deviation of the particle from the horizontal orbit; thus, the total effect is quadratic in the deviation, i.e., proportional to the horizontal (radial) beam size:

$$\frac{\Delta\omega_a}{\omega_a} = -2\beta^2 n(1-n)\,\frac{\langle x^2\rangle}{R_0^2}\,.$$

The beam size was determined from the debunching analysis. The correction was slightly different for different runs; for example, in 2001, the correction was -0.47 ± 0.054 ppm.

The main contributions to the systematic measurement error of ω_a for the three seasons during which most of the statistics were obtained are listed in Table 4.

To reconstruct the events from the data of the experiment detectors, two independent codes written in different languages and using different libraries were designed. The 'row' experimental data were doubled. Full reconstruction using data from one copy was performed using the BNL computer facilities. Full reconstruction from the second copy was performed using facilities of the National Center for Supercomputing Applications (NCSA, USA). The results of both reconstructions were matched. Two independent data processing codes allowed avoiding systematic errors due to possible bugs in the codes.

The data analysis was organized so as to prevent any bias. The analysis was performed by several experimental groups, each of which analyzed data from one run reconstructed by one of the codes and using one of the several methods described above. During data analysis, the results obtained by different groups were discussed and compared. To avoid influencing each other, the measurements of the frequency ω_a by each group were shifted by a small number of the order of 10 ppm. Moreover, two shifts were used: a common one known to each group processing the calorimeter data but unknown to the groups measuring the proton precession frequency ω_p, and an individual one, known only to members of the corresponding group. This made it impossible to compare the precession frequencies obtained by different groups but enabled a comparison of various systematic effects, for example, the dependence of the

Table 4. Systematic errors for the precession frequency ω_a. For 2001 data, the total systematic error from contributions marked with * is 0.11 ppm.

Systematic error source	1999	2000	2001
Energy calibration stability	0.02	0.13	0.12
Pileup	0.13	0.13	0.08
Coherent betatron oscillations	0.05	0.21	0.07
AGS background	0.10	0.01	*
Lost muons	0.10	0.10	0.09
Timing shifts	0.10	0.02	*
E field and betatron oscillation corrections	0.08	0.06	0.03
Fitting procedure	0.07	0.06	*
Total systematic error of ω_a	0.3	0.31	0.21

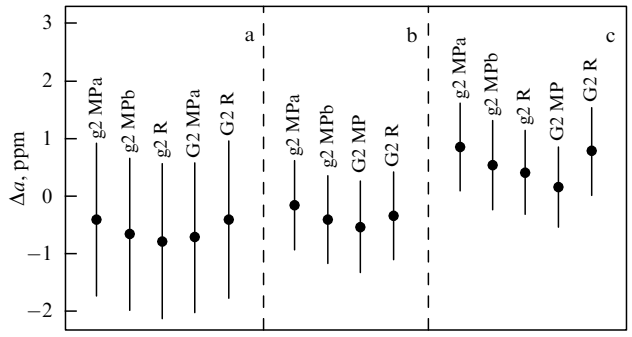

Figure 34. Comparison of individual data analyses performed in the (a) 1999, (b) 2000, and (c) 2001 runs. To describe the analysis method, the following notation is used: g2/G2 — the row event production by g2too/g2off tools, MP/R — analysis based on the $N(t)/r(t)$ approximation [27].

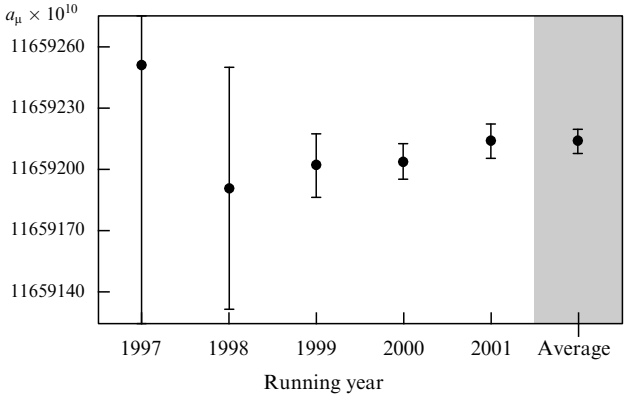

Figure 35. Muon anomalous magnetic moment as measured from the data taken in 1997–2001. The dot on the right shows the final average obtained from the 1999–2001 data [27].

frequency on the threshold energy or the run number. Each group had to be able to demonstrate the stability of the obtained results, for example, that the value of χ^2/v is consistent with unity, the value of ω_a is independent of the time interval after the injection within which $N(t)$ is approximated, and the results obtained for different data subsets (in particular, for individual detectors) are consistent with each other. After the completion of data analysis by different groups, the individual shifts were removed to determine the unique value of ω_a. Here, the common shift remained, and it was removed only after the completion of both ω_a and ω_p measurements.

Figure 34 shows the results of 14 different data analyses collected during the 1999, 2000, and 2001 running periods. Different analyses of data collected in one run use essentially the same statistics. However, the overlapping is not perfect: differences in the data sets amounted to 10%. Taking these differences into account, the results of the data analyses are consistent.

Using the relations

$$\omega_a = \frac{e}{m_\mu}\, a_\mu B\,, \quad \hbar\omega_p = 2\mu_p B\,,$$

$$\mu_\mu = g_\mu\, \frac{e\hbar}{4m_\mu} = (1 + a_\mu)\, \frac{e\hbar}{2m_\mu}\,,$$

it is easy to express the muon anomalous magnetic moment as

$$a_\mu = \frac{\omega_a/\omega_p}{\mu_\mu/\mu_p - \omega_a/\omega_p}\,. \tag{76}$$

The value of the constant $\mu_\mu/\mu_p = 3.18334539(10)$ is measured with high precision in a separate experiment [197] and improved in a global analysis of physical constants [198]. This value was used to determine a_μ in the discussed experiment. Later on, the accuracy of determining μ_μ/μ_p was increased [83]. The new value $\mu_\mu/\mu_p = 3.183345142(71)$ is consistent with the previous measurements. A recalculation of the experimental results using the new value of μ_μ/μ_p leads to a small shift, which is insignificant within the measurement errors.

To determine a_μ, the ratio of the measured values of ω_a and ω_p was used; here, in the ω_p measurements, only those time intervals inside which data were acquired were taken into account. In addition, in time averaging of the magnetic field, the data were weighted in accordance with the statistics collected by the calorimeters within a particular time interval.

Figure 35 shows the results of measurements of the muon anomalous magnetic moment using data taken in each run [164, 185, 199–201]. To obtain the final result, the results of the 1999–2001 runs were averaged. The results of the 1997 and 1998 runs were not taken into account for two reasons: first, their statistical contribution to the final result is negligible; second, in the analysis of these data, part of the systematic corrections were ignored, which increased the corresponding systematic error.

When averaging the 1999–2001 results, the correlation between the contributions to the systematic error for different runs was taken into account. The following factors were assumed to be the same for all runs: the accuracy of the absolute calibration of the magnetic field, the difference between the spin direction of the lost muons and the spin of the main ensemble of muons, and the uncertainty of the corrections due to the electric field and betatron oscillations. For the remaining contributions to the systematic error, the value of the error was assumed to be independent in each run.

As noted above, after the publication of [27], the value of the constant μ_μ/μ_p was improved. The use of its new value leads to a small shift of the result by approximately 1/5 of the full error:

$$a_\mu(\text{E821}) = 11659208.9(6.3) \times 10^{-10} \quad (0.54\ \text{ppm})\,. \tag{77}$$

In 1999 and 2000, measurements were performed for positively charged muons, and in 2001 for negatively charged muons. Averaging these three runs is possible only if the CPT symmetry is assumed: in this case, $a_{\mu^+} \equiv a_{\mu^-}$. The obtained results

$$\frac{\omega_a}{\omega_p}\,(\mu^+) = 0.0037072047(26)\,,$$

$$\frac{\omega_a}{\omega_p}\,(\mu^-) = 0.0037072083(26)$$

are consistent with the CPT invariance:

$$\frac{\omega_a}{\omega_p}\,(\mu^+) - \frac{\omega_a}{\omega_p}\,(\mu^-) = (36 \pm 37) \times 10^{-10}\,.$$

The difference between measurements of a_μ in the E821 experiment (77) and the SM prediction (54) is

$$\Delta a_\mu = a_\mu(\text{E821}) - a_\mu(\text{SM}) = (268 \pm 77) \times 10^{-11} \quad (3.5\sigma)\,. \tag{78}$$

Other calculations of the strong interaction contributions result in a somewhat different $a_\mu(\text{SM})$, but this does not alter the general picture: the difference between the measured and calculated values typically remains within 3.5–4.3 standard deviations.

4. Prospects. Conclusion

Figure 36 shows a comparison of the measurement uncertainty of a_μ achieved in the described experiments with contributions of the various interactions. In a series of a_μ measurements at CERN, the QED contribution was tested at an increasing level of precision, and the sensitivity of the CERN III experiment allowed identifying the hadronic contribution. The accuracy of the most precise measurement today, the E821 experiment at BNL, requires taking the contributions from all known interactions into account.

The results of the E821 measurements of the muon anomalous magnetic moment and a broad program of measurements of hadron cross sections suggest that the difference between the measured value of a_μ and its calculated SM value is at a level of 3.5–4 standard deviations. Considering the complexity of the experiments and calculations, such a discrepancy cannot be interpreted as a reliable indication of the existence of interactions beyond the Standard Model. However, the obtained result aroused great interest from the scientific community and stimulated new experimental efforts to increase the statistical significance of the result.

Presently, two experiments aimed at improving the measurement accuracy of the muon anomalous magnetic moment are under preparation. The E989 experiment at Fermilab [202, 203] generally follows the layout of the CERN III and E821 experiments; however, thanks to improvements in almost all experimental components and an order-of-magnitude larger statistics, a relative uncertainty of 0.14 ppm is expected, which is a factor of four better than that of E821. By the beginning of 2018, the experiment was almost ready to start data taking scheduled for two years.

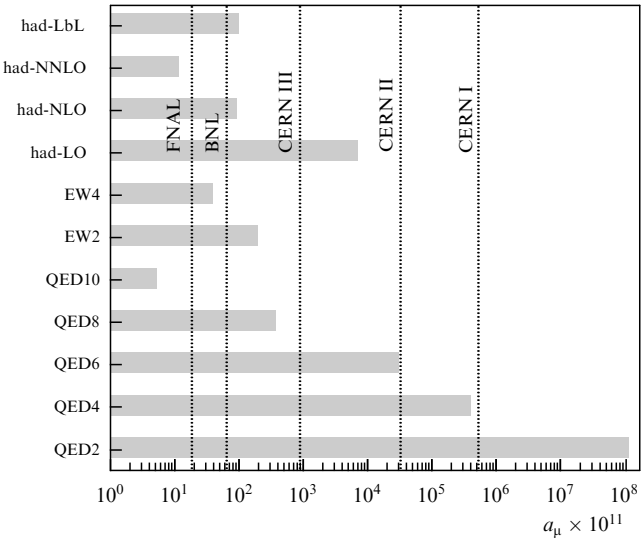

Figure. 36. Comparison of the accuracy of measurements of the muon anomalous magnetic moment and the value of contributions to it from separate interactions.

The second experiment, E34, is planned at J-PARC (Japan Proton Accelerator Research Complex) (Japan) [204] and is very different from the traditional setup. An ultra-cold muon beam is proposed to be used, which will make it possible to discard electrostatic focusing and to perform measurements with much lower muon momenta. Thanks to this, systematic measurement errors at Fermilab and J-PARC will be almost independent. The E34 experiment is now at the research and development stage. At the first stage, the BNL measurement uncertainty is to be reached.

The prospects for new measurements of a_μ (and also of a_e) in the early 1990s stimulated the development of theoretical calculations of the muon anomalous magnetic moment, which led to significant progress in the field. In particular,

(1) the fifth-order electromagnetic contribution was calculated complerely;

(2) the next-to-leading-order weak interaction contribution was calculated completely;

(3) hadron cross sections were directly measured at the VEPP-2M collider;

(4) a new method to measure hadron cross sections at e^+e^- factories, the initial-state radiation method, was developed; and

(5) a method to calculate the light-by-light scattering reached a new level.

Similarly, the prospects to further increase the measurement accuracy of the muon anomalous magnetic moment in experiments at Fermilab and J-PARC are greatly stimulating further development of theoretical calculations of a_μ. The expected uncertainty of the E989 experiment corresponds to 1/10 of the contribution due to weak interactions a_μ^{EW}, or 1/400 of the leading-order strong interaction contribution $a_\mu^{\text{had, LO}}$, or 1/7 of the light-by-light scattering contribution $a_\mu^{\text{had, LO}}$. In order to match the measurement errors, the calculation uncertainty should be 16×10^{-11}, around a factor of three better than the current value 45×10^{-11} (54).

We outline the main avenues of the development of the calculations. The calculation uncertainty of contributions due to electromagnetic and weak interactions, 0.034×10^{-11} and 1.0×10^{-11}, respectively, is more than enough to compare with the new measurements. However, the fourth- and fifth-order electromagnetic contributions, which jointly amount to 386×10^{-11}, are mainly calculated by numerical integration. Therefore, an independent calculation of these contributions is very important in order to enhance the reliability of the calculations. This work is now under way: as discussed above, the universal fourth-order contribution was calculated completely by a semianalytic method, and a significant proportion of the diagrams was calculated analytically.

The theoretical uncertainty of a_μ is determined by the contribution due to strong interactions. The hadron vacuum polarization and light-by-light scattering contribute about equally to the calculation error, although the former contribution is two orders of magnitude larger than the latter.

The hadron vacuum polarization accuracy is determined by measurement errors of hadron cross sections. Presently, experiments at the VEPP-2000 e^+e^- collider [35, 205] with the CMD-3 [36, 38, 206–214] and SND [215–227] detectors

continue. The goal of these experiments is to perform direct measurements of hadron cross sections with large statistics and a low systematic error. This will allow both an improvement in the statistical uncertainty of the hadron contribution calculations and a detailed comparison of the direct measurements with the initial-state radiation measurements, which currently dominate the calculation. At the same time, lattice QCD calculations of $a_\mu^{\mathrm{had,LO}}$ are actively developing. At least three independent calculations with an uncertainty of 0.3–0.5% can be expected within several years: using the VEPP-2000 data, using the ISR measurements, and using lattice QCD calculations. The independent calculations will enable us to justify the reliability of the calculations with high accuracy, and the uncertainty of the joint result can reach 0.2–0.3%, which will match the measurement errors of a_μ.

We note yet another possibility to determine $a_\mu^{\mathrm{had,LO}}$, by using dispersion relations similar to (33) but in the space-like region. Corresponding experiments have been proposed [228, 229], and their possible realization is presently under study.

The major progress in calculating the light-by-light scattering contribution is expected from lattice QCD calculations. In addition, a more traditional method based on the use of effective models is actively being developed. Here, the accuracy increase is expected thanks to the use of double-photon hadron form factors, which are planned to be measured in the KLOE-2 and BES-III experiments. Generally, a 10% accuracy increase can be expected in several years.

The calculation of the muon anomalous magnetic moment in the Standard Model is a very active field. In the next five years, during which new measurements of a_μ at Fermilab are expected, the theoretical calculation accuracy can hopefully be increased by a factor of 1.5–3. With the improved measurement uncertainty, the expected error in $\Delta a_\mu = a_\mu(\mathrm{E989}) - a_\mu(\mathrm{SM})$ can be $(20-35)\times 10^{-11}$, which is a factor of 2 to 4 better than the current uncertainty. With the value of Δa_μ preserved, such an uncertainty will correspond to the confirmation of a nonzero value of Δa_μ to within seven or more standard deviations.

Acknowledgements

The work by I B L is supported by the Russian Foundation for Basic Research (grant 17-02-00847). The work by S I E is supported by a grant from the Government of the Russian Federation for support of scientific research supervised by leading scientists (contract No. 14.W03.31.0026 dated 15.02.2018).

References

1. Gerlach W, Stern O *Z. Phys.* **9** 353 (1922)
2. Goudschmidt S A, Uhlenbeck G H *Nature* **117** 264 (1926)
3. Fraser R G J *Proc. R. Soc. Lond. A* **114** 212 (1927)
4. Compton A H *J. Franklin Inst.* **192** 145 (1921)
5. Dirac P A M *Proc. R. Soc. Lond. A* **117** 610 (1928)
6. Nafe J E, Nelson E B, Rabi I I *Phys. Rev.* **71** 914 (1947)
7. Kusch P, Foley H M *Phys. Rev.* **72** 1256 (1947)
8. Schwinger J S *Phys. Rev.* **73** 416 (1948)
9. Schwinger J S *Phys. Rev.* **76** 790 (1949)
10. Lamb W E, Retherford R C *Phys. Rev.* **72** 241 (1947)
11. Rich A, Wesley J C *Rev. Mod. Phys.* **44** 250 (1972)
12. Van Dyck R S, Schwinberg P B, Dehmelt H G *Phys. Rev. Lett.* **59** 26 (1987)
13. Hanneke D, Fogwell S, Gabrielse G *Phys. Rev. Lett.* **100** 120801 (2008); arXiv:0801.1134
14. Hanneke D, Hoogerheide S F, Gabrielse G *Phys. Rev. A* **83** 052122 (2011); arXiv:1009.4831
15. Lee T D, Yang C N *Phys. Rev.* **104** 254 (1956)
16. Garwin R L, Lederman L M, Weinrich M *Phys. Rev.* **105** 1415 (1957)
17. Garwin R L et al. *Phys. Rev.* **118** 271 (1960)
18. Berestetskii V B, Krokhin O P, Khlebnikov A K *Sov. Phys. JETP* **3** 761 (1956); *zh. Eksp. Teor. Fiz.* **30** 788 (1956)
19. Glashow S L *Nucl. Phys.* **22** 579 (1961)
20. Weinberg S *Phys. Rev. Lett.* **19** 1264 (1967)
21. Salam A "Weak and electromagnetic interactions", in *Elementary Particle Theory. Proc. 8th Nobel Symp., 19 – 25 May 1968, Lerum, Sweden* (Ed. N Svartholm) (New York: Wiley; Stockholm: Almqvist and Wiksell, 1968) p. 367
22. Charpak G rt al. *Phys. Rev. Lett.* **6** 128 (1961)
23. Charpak G, Farley F J M, Garwin R L *Phys. Lett.* **1** 16 (1962)
24. Bailey J et al. *Phys. Lett. B* **28** 287 (1968)
25. Bailey J et al. (CERN Muon Storage Ring) *Phys. Lett. B* **55** 420 (1975)
26. Bailey J et al. (CERN-Mainz-Daresbury) *Nucl. Phys. B* **150** 1 (1979)
27. Bennett G W et al. (Muon g-2) *Phys. Rev. D* **73** 072003 (2006); hep-ex/0602035
28. Aoyama T et al. *Phys. Rev. Lett.* **109** 111808 (2012); arXiv:1205.5370
29. Czarnecki A, Krause B, Marciano W J *Phys. Rev. Lett.* **76** 3267 (1996); hep-ph/9512369
30. Gnendiger C, Stockinger D, Stockinger-Kim H *Phys. Rev. D* **88** 053005 (2013); arXiv:1306.5546
31. Hagiwara K et al. *J. Phys. G* **38** 085003 (2011); arXiv:1105.3149
32. Davier M et al. *Eur. Phys. J. C* **71** 1515 (2011); *Eur. Phys. J. C* **72** 1874 (2012); arXiv:1010.4180
33. Anashkin E V et al. *Instrum. Exp. Tech.* **49** 798 (2006); *Prib. Tekh. Eksp.* **49** 63 (2006)
34. Achasov M N et al. *Nucl. Instrum. Meth. Phys. Res. A* **449** 125 (2000); hep-ex/9909015
35. Shatunov P Yu et al. *Phys. Part. Nucl. Lett.* **13** 995 (2016)
36. Khazin B, in *PHIPSI08, Proc. Inter. Workshop on* e^+e^- *Collisions from Phi to Psi, Frascati, Italy, 7 – 10 April 2008*; *Nucl. Phys. Proc. Suppl.* **181 – 182** 376 (2008)
37. Achasov M N et al., in *Proc. of the 10th Intern. Conf. on Instruments for Colliding Beam Physics, INSTR08, Novosibirsk, Russia, February 28 – March 5, 2008*; *Nucl. Instrum. Meth. Phys. Res. A* **598** 31 (2009)
38. Logashenko I B (CMD-3, SND), in *Proc. of the 38th Intern. Conf. on High Energy Physics, ICHEP 2016*: *Chicago, IL, USA, August 3 – 10, 2016*; PoS **ICHEP2016** 544 (2016)
39. Aubert B et al. (BaBar) *Nucl. Instrum. Meth. Phys. Res. A* **479** 1 (2002); hep-ex/0105044
40. Abashian A et al. *Nucl. Instrum. Meth. Phys. Res. A* **479** 117 (2002)
41. Adinolfi M et al. *Nucl. Instrum. Meth. Phys. Res. A* **488** 51 (2002)
42. Adinolf Mi et al. *Nucl. Instrum. Meth. Phys. Res. A* **482** 364 (2002)
43. Druzhinin V P, Eidelman S I, Serednyakov S I, Solodov E P *Rev. Mod. Phys.* **83** 1545 (2011); arXiv:1105.4975
44. Davier M et al. *Eur. Phys. J. C* **77** 827 (2017); arXiv:1706.09436
45. Jegerlehner F *Springer Tracts Mod. Phys.* **274** 1 (2017)
46. Kinoshita T, Nizic B, Okamoto Y *Phys. Rev. D* **41** 593 (1990)
47. Petermann A *Helv. Phys. Acta* **30** 407 (1957)
48. Sommerfield S M *Phys. Rev.* **107** 328 (1957)
49. Petermann A *Phys. Rev.* **105** 1931 (1957)
50. Suura H, Wichmann E H *Phys. Rev.* **105** 1930 32 (1957)
51. Elend H *Phys. Lett.* **20** 682 (1966)
52. Passera M *J. Phys. G* **31** R75 (2005)
53. Passera M *Phys. Rev. D* **75** 013002 (2007); hep-ph/0606174
54. Kinoshita T *Adv. Ser. Direct. High Energy Phys.* **7** 218 (1990)
55. Laporta S, Remiddi E *Phys. Lett. B* **379** 283 (1996); hep-ph/9602417
56. Laporta S *Nuovo Cimento A* **106** 675 (1993)
57. Laporta S, Remiddi E *Phys. Lett. B* **301** 440 (1993)
58. Czarnecki A, Skrzypek M *Phys. Lett. B* **449** 354 (1999); hep-ph/9812394
59. Friot S, Greynat D, De Rafael E *Phys. Lett. B* **628** 73 (2005); hep-ph/0505038
60. Kinoshita T, Lindquist W B *Phys. Rev. D* **27** 867 (1983)
61. Kinoshita T, Lindquist W B *Phys. Rev. D* **27** 877 (1983)

62. Kinoshita T, Lindquist W B *Phys. Rev. D* **27** 886 (1983)
63. Kinoshita T, Lindquist W B *Phys. Rev. D* **39** 2407 (1989)
64. Kinoshita T, Lindquist W B *Phys. Rev. D* **42** 636 (1990)
65. Kinoshita T, Nio M *Phys. Rev. D* **73** 013003 (2006); hep-ph/0507249
66. Aoyama T et al. *Phys. Rev. Lett.* **99** 110406 (2007); arXiv:0706.3496
67. Aoyama T et al. *Phys. Rev. D* **77** 053012 (2008); arXiv:0712.2607
68. Aoyama T et al. *Phys. Rev. Lett.* **109** 111807 (2012); arXiv:1205.5368
69. Aoyama T et al. *Phys. Rev. D* **91** 033006 (2015); arXiv:1412.8284
70. Caffo M, Turrini S, Remiddi E *Phys. Rev. D* **30** 483 (1984)
71. Laporta S *Phys. Lett. B* **772** 232 (2017); arXiv:1704.06996
72. Helaman D H B, Ferguson R P, Arno S *Math. Comput.* **68** 351 (1999)
73. Kinoshita T, Nio M *Phys. Rev. D* **70** 113001 (2004); hep-ph/0402206
74. Faustov R N et al. *Phys. Lett. B* **254** 241 (1991)
75. Broadhurst D J, Kataev A L, Tarasov O V *Phys. Lett. B* **298** 445 (1993); hep-ph/9210255
76. Laporta S *Phys. Lett. B* **312** 495 (1993); hep-ph/9306324
77. Laporta S, Mastrolia P, Remiddi E *Nucl. Phys. B* **688** 165 (2004); hep-ph/0311255
78. Kataev A L *Phys. Lett. B* **284** 401 (1992); *Phys. Lett. B* **710** 710 (2012)
79. Karshenboim S G *Phys. Atom. Nucl.* **56** 857 (1993); *Yad. Fiz.* **56** (6) 252 (1993)
80. Laporta S *Phys. Lett. B* **328** 522 (1994); hep-ph/9404204
81. Kataev A L, Starshenko V V *Phys. Rev. D* **52** 402 (1995); hep-ph/9412305
82. Baikov P A et al. *Nucl. Phys. B* **867** 182 (2013); arXiv:1207.2199
83. Mohr P J, Newell D B, Taylor B N *Rev. Mod. Phys.* **88** 035009 (2016); arXiv:1507.07956
84. Bardeen W A, Gastmans R, Lautrup B E *Nucl. Phys. B* **46** 319 (1972)
85. Jackiw R, Weinberg S *Phys. Rev. D* **5** 2396 (1972)
86. Bars I, Yoshimura M *Phys. Rev. D* **6** 374 (1972)
87. Fujikawa K Lee B W, Sanda A I *Phys. Rev. D* **6** 2923 (1972)
88. 't Hooft G *Nucl. Phys. B* **33** 173 (1971)
89. 't Hooft G, Veltman M J G *Nucl. Phys. B* **44** 189 (1972)
90. Kukhto T V et al. *Nucl. Phys. B* **371** 567 (1992)
91. Adler S L *Phys. Rev.* **177** 2426 (1969)
92. Bell J S, Jackiw R *Nuovo Cimento A* **60** 47 (1969)
93. Bardeen W A *Phys. Rev.* **184** 1848 (1969)
94. Peris S, Perrottet M, de Rafael E *Phys. Lett. B* **355** 523 (1995); hep-ph/9505405
95. Czarnecki A, Krause B, Marciano W J *Phys. Rev. D* **52** R2619 (1995); hep-ph/9506256
96. Degrassi G, Giudice G F *Phys. Rev. D* **58** 053007 (1998); hep-ph/9803384
97. Czarnecki A, Marciano W J, Vainshtein A *Phys. Rev. D* **67** 073006 (2003); *Phys. Rev. D* **73** 119901 (2006); hep-ph/0212229
98. Aad G et al. (ATLAS), *Phys. Lett. B* **716** 1 (2012); arXiv:1207.7214
99. Chatrchyan S et al. (CMS) *Phys. Lett. B* **716** 30 (2012); arXiv:1207.7235
100. Bouchiat C, Michel L *J. Phys. Radium* **22** 121 (1961)
101. Durand L *Phys. Rev.* **128** 441 (1962)
102. Kinoshita T, Oakes R J *Phys. Lett. B* **25** 143 (1967)
103. Gourdin M, De Rafael E *Nucl. Phys. B* **10** 667 (1969)
104. Brodsky S J, De Rafael E *Phys. Rev.* **168** 1620 (1968)
105. Jegerlehner F, in *Fifty Years of Electroweak Physics. Proc. of the Symp. in Honour of Professor Alberto Sirlin's 70th Birthday, New York, USA, October 27–28, 2000*; *J. Phys. G* **29** 101 (2003); hep-ph/0104304
106. Anastasi A et al. (KLOE-2) *Phys. Lett. B* **767** 485 (2017); arXiv:1609.06631
107. Baikov P A, Chetyrkin K G, Kuhn J H *Phys. Rev. Lett.* **101** 012002 (2008); arXiv:0801.1821
108. Anashin V V et al. *Phys. Lett. B* **770** 174 (2017); arXiv:1610.02827
109. Anashin V V et al. *Phys. Lett. B* **753** 533 (2016); arXiv:1510.02667
110. Bai J Z et al. (BES) *Phys. Rev. Lett.* **88** 101802 (2002); hep-ex/0102003
111. Ablikim M et al. (BES) *Phys. Lett. B* **677** 239 (2009); arXiv:0903.0900
112. Auslander V L et al. *Phys. Lett. B* **25** 433 (1967)
113. Augustin J E et al. *Phys. Lett. B* **28** 508 (1969)
114. Augustin J E et al. *Phys. Lett. B* **28** 513 (1969)
115. Augustin J E et al. *Phys. Lett. B* **28** 517 (1969)
116. Barkov L M et al. *Nucl. Instrum. Meth. Phys. Res.* **204** 379 (1983)
117. Dolinsky S I et al. *Phys. Rep.* **202** 99 (1991)
118. Barkov L M et al. *Nucl. Phys. B* **256** 365 (1985)
119. Akhmetshin R R et al. (CMD-2) *Phys. Lett. B* **527** 161 (2002); hep-ex/0112031
120. Akhmetshin R R et al. (CMD-2) *Phys. Lett. B* **578** 285 (2004); hep-ex/0308008
121. Aulchenko V M et al. (CMD-2) *JETP Lett.* **82** 33 743 (2005); *Pis'ma Zh. Eksp. Teor. Fiz.* **82** 841 (2005); hep-ex/0603021
122. Akhmetshin R R et al. *JETP Lett.* **84** 413 (2006); *Pis'ma Zh. Eksp. Teor. Fiz.* **84** 491 (2006); hep-ex/0610016
123. Akhmetshin R R et al. (CMD-2) *Phys. Lett. B* **648** 28 (2007); hep-ex/0610021
124. Tsai Y-S *Phys. Rev. D* **4** 2821 (1971); *Phys. Rev. D* **13** 771 (1976)
125. Marciano W J, Sirlin A *Phys. Rev. Lett.* **56** 22 (1986)
126. Eidelman S I, Ivanchenko V N *Phys. Lett. B* **257** 437 (1991)
127. Barate R et al. (ALEPH) *Z. Phys. C* **76** 15 (1997)
128. Alemany R, Davier M, Hocker A *Eur. Phys. J. C* **2** 123 (1998); hep-ph/9703220
129. Fujikawa M et al. (Belle), *Phys. Rev. D* **78** 072006 (2008); arXiv:0805.3773
130. Jegerlehner F, Szafron R *Eur. Phys. J. C* **71** 1632 (2011); arXiv:1101.2872
131. Arbuzov A V et al. *JHEP* **12** 009 (1998); hep-ph/9804430
132. Binner S, Kuhn J H, Melnikov K *Phys. Lett. B* **459** 279 (1999); hep-ph/9902399
133. Benayoun M, Eidelman S I, Ivanchenko V N, Silagadze Z K, in *Hadron Spectroscopy. Proc., Workshop, Frascati, Italy, March 8–12, 1999*; *Mod. Phys. Lett. A* **14** 2605 (1999); hep-ph/9910523
134. Actis S et al. (Working Group on Radiative Corrections and Monte Carlo Generators for Low Energies), *Eur. Phys. J. C* **66** 585 (2010); arXiv:0912.0749
135. Aubert B et al. (BaBar) *Phys. Rev. Lett.* **103** 231801 (2009); arXiv:0908.3589
136. Lees J P et al. (BaBar) *Phys. Rev. D* **86** 032013 (2012); arXiv:1205.2228
137. Ambrosino F et al. (KLOE) *Phys. Lett. B* **670** 285 (2009) arXiv:0809.3950
138. Ambrosino F et al. (KLOE) *Phys. Lett. B* **700** 102 (2011); arXiv:1006.5313
139. Babusci D et al. (KLOE) *Phys. Lett. B* **720** 336 (2013); arXiv:1212.4524
140. Ablikim M et al. (BESIII) *Phys. Lett. B* **753** 629 (2016); arXiv:1507.08188
141. Eidelman S, Jegerlehner F *Z. Phys. C* **67** 585 (1995); hep-ph/9502298
142. Kinoshita T, Nizic B, Okamoto Y *Phys. Rev. Lett.* **52** 717 (1984)
143. Narison S *J. Phys. G* **4** 1849 (1978)
144. Martinovic L, Dubnicka S *Phys. Rev. D* **42** 884 (1990)
145. Davier M, Hocker A *Phys. Lett. B* **419** 419 (1998); hep-ph/9801361
146. Davier M, Eidelman S, Hocker A, Zhang Z *Eur. Phys. J. C* **31** 503 (2003); hep-ph/0308213
147. Hagiwara K et al. *Phys. Rev. D* **69** 093003 (2004); hep-ph/0312250
148. Davier M et al. *Eur. Phys. J. C* **66** 1 (2010); arXiv:0908.4300
149. Lehner C, in *35th Intern. Symp. on Lattice Field Theory, Lattice 2017, Granada, Spain, June 18–24, 2017* (2017); arXiv:1710.06874
150. Chakraborty B et al. *Phys. Rev. D* **96** 034516 (2017), arXiv:1601.03071
151. Blum T et al. *Phys. Rev. Lett.* **116** 232002 (2016); arXiv:1512.09054
152. Krause B *Phys. Lett. B* **390** 392 (1997); hep-ph/9607259
153. Kurz A et al. *Phys. Lett. B* **734** 144 (2014); arXiv:1403.6400
154. Kurz A et al., in *Proc. of the Workshop on Flavour Changing and Conserving Processes 2015* (*FCCP2015*): *Anacapri, Capri Island, Italy, September 10–12, 2015*; *EPJ Web Conf.* **118** 01033 (2016); arXiv:1511.08222
155. Melnikov K, Vainshtein A *Springer Tracts Mod. Phys.* **216** 1 (2006)
156. Hayakawa M, Kinoshita T, Sanda A I *Phys. Rev. Lett.* **75** 790 (1995); hep-ph/9503463
157. Hayakawa M, Kinoshita T, Sanda A I *Phys. Rev. D* **54** 3137 (1996); hep-ph/9601310
158. Hayakawa M, Kinoshita T *Phys. Rev. D* **57** 465 (1998); *Phys. Rev. D* **66** 019902 (2002); hep-ph/9708227
159. Bijnens J, Pallante E, Prades J *Nucl. Phys. B* **474** 379 (1996); hep-ph/9511388
160. Bijnens J, Pallante E, Prades J *Phys. Rev. Lett.* **75** 1447 (1995); *Phys. Rev. Lett.* **75** 3781 (1995); hep-ph/9505251

161. Knecht M , Nyffeler A *Phys. Rev. D* **65** 073034 (2002); hep-ph/0111058
162. Knecht M et al. *Phys. Rev. Lett.* **88** 071802 (2002); hep-ph/ 0111059
163. Melnikov K, Vainshtein A *Phys. Rev. D* **70** 113006 (2004); hep-ph/0312226
164. Brown H N et al. (Muon g-2) *Phys. Rev. Lett.* **86** 2227 (2001); hep-ex/0102017
165. Prades J, de Rafael E, Vainshtein A *Adv. Ser. Direct. High Energy Phys.* **20** 303 (2009); arXiv:0901.0306
166. Jegerlehner F, Nyffeler A *Phys. Rep.* **477** 1 (2009); arXiv:0902.3360
167. Colangelo G et al. *Phys. Lett. B* **735** 90 (2014); arXiv:1403.7512
168. Larin I et al. (PrimEx) *Phys. Rev. Lett.* **106** 162303 (2011); arXiv:1009.1681
169. Behrend H J et al. (CELLO) *Z. Phys. C* **49** 401 (1991)
170. Gronberg J et al. (CLEO) *Phys. Rev. D* **57** 33 (1998); hep-ex/9707031
171. Aubert B et al. (BaBar) *Phys. Rev. D* **80** 052002 (2009); arXiv:0905.4778
172. Uehara S et al. (Belle) *Phys. Rev. D* **86** 092007 (2012); arXiv:1205.3249
173. Babusci D et al. *Eur. Phys. J. C* **72** 1917 (2012); arXiv:1109.2461
174. Blum T et al., arXiv:1311.2198
175. Hayakawa M et al., in *Proc. of the 23rd Intern. Symp. on Lattice Field Theory, Lattice 2005*, *Dublin, Ireland, July 25 – 30, 2005, PoS* **LAT2005** 353 (2006); hep-lat/0509016
176. Blum T et al. *Phys. Rev. Lett.* **114** 012001 (2015); arXiv:1407.2923
177. Blum T et al. *Phys. Rev. D* **93** 014503 (2016); arXiv:1510.07100
178. Blum T et al. *Phys. Rev. Lett.* **118** 022005 (2017); arXiv:1610.04603
179. Green J et al. *Phys. Rev. Lett.* **115** 222003 (2015); arXiv:1507.01577
180. Gerardin A, Meyer H B, Nyffeler A *Phys. Rev. D* **94** 074507 (2016); arXiv:1607.08174
181. Gerardin A, Meyer H B, Nyffeler A, in *Proc. of the 34th Intern. Symp. on Lattice Field Theory, Lattice 2016, Southampton, UK, July 24 – 30, 2016*; *PoS* **LATTICE2016** 175 (2016); arXiv:1611.02190
182. Charpak G et al. *Nuovo Cimento* **37** 1241 (1965)
183. Okun L P *Leptons and Quarks* (Singapore, NJ: World Scientific, 2014); Translated from Russian: *Leptony i Kvarki* (Moscow: Nauka, 1990)
184. Farley F J M, Picasso E *Adv. Ser. Direct. High Energy Phys.* **7** 479 (1990)
185. Carey R M et al. *Phys. Rev. Lett.* **82** 1632 (1999)
186. Krienen F, Loomba D, Meng W *Nucl. Instrum. Meth. Phys. Res. A* **283** 5 (1989)
187. Yamamoto A et al. *Nucl. Instrum. Meth.Phys. Res. A* **491** 23 (2002)
188. Efstathiadis E et al. *Nucl. Instrum. Meth. Phys. Res. A* **496** 8 (2003)
189. Semertzidis Y K et al. *Nucl. Instrum. Meth. Phys. Res. A* **503** 458 (2003)
190. Danby G T et al. *Nucl. Instrum. Meth. Phys. Res. A* **457** 151 (2001)
191. Prigl R et al. *Nucl. Instrum. Meth. Phys. Res. A* **374** 118 (1996)
192. Fei X, Hughes V W, Prigl R *Nucl. Instrum. Meth. Phys. Res. A* **394** 349 (1997)
193. Neronov Y I, Seregin N N *Metrologia* **51** 54 (2014)
194. Sedykh S A et al. *Nucl. Instrum. Meth. Phys. Res. A* **455** 346 (2000)
195. Farley F J N *Phys. Lett. B* **42** 66 (1972)
196. Paley J, Ph.D. Thesis (Boston Univ., 2004)
197. Liu W et al. *Phys. Rev. Lett.* **82** 711 (1999)
198. Mohr P J, Taylor B N *Rev. Mod. Phys.* **72** 351 (2000)
199. Brown H N et al. (Muon (g-2)) *Phys. Rev. D* **62** 091101 (2000); hep-ex/0009029
200. Bennett G W et al. (Muon g-2) *Phys. Rev. Lett.* **89** 101804 (2002); *Phys. Rev. Lett.* **89**129903 (2002); hep-ex/0208001
201. Bennett G W et al. (Muon g-2) *Phys. Rev. Lett.* **92** 161802 (2004); hep-ex/0401008
202. Grange J et al. (Muon g-2), arXiv:1501.06858
203. Logashenko I et al. (Muon g-2) *J. Phys. Chem. Ref. Data* **44** 031211 (2015)
204. Saito N (J-PARC g-2/EDM), *Proc. of the Intern. Workshop on Grand Unified Theories* (*GUT2012*): *Kyoto, Japan, March 15 – 17, 2012*; *AIP Conf. Proc.* **1467** 45 (2012)
205. Berkaev D et al., in *Proc. of the 8th Intern. Workshop on* e^+e^- *Collisions from Phi to Psi* (*PHIPSI11*): *Novosibirsk, Russia, September 19 – 22, 2011; Nucl. Phys. Proc. Suppl.* **225 – 227** 303 (2012)
206. Logashenko I B et al., in *Proc. Intern. Symp. on Lepton and Hadron Physics at Meson-Factories, LHPMF 2013, Messina, Italy, October 13 – 15, 2013*; *EPJ Web Conf.* **72** 00013 (2014)
207. Akhmetshin R R et al. (CMD-3), in *Proc. of the Intern. Conference on Instrumentation for Colliding Beam Physics* (*INSTR17*), *Novosibirsk, Russia*; *JINST* **12** C07044 (2017)
208. Akhmetshin R R et al. (CMD-3) *Phys. Lett. B* **773** 150 (2017); arXiv:1706.06267
209. Kozyrev E A et al. (CMD-3) *Phys. Lett. B* **760** 314 (2016); arXiv:1604.02981
210. Akhmetshin R R et al. (CMD-3) *Phys. Lett. B* **759** 634 (2016); arXiv:1507.08013
211. Akhmetshin R R et al. (CMD-3) *Phys. Lett. B* **723** 82 (2013); arXiv:1302.0053
212. Akhmetshin R R et al., in *Proc. of the 17th Intern. Conf. on Calorimetry in Particle Physics* (*CALOR 2016*): *Daegu, Republic of Korea, May 15-20, 2016*; *J. Phys. Conf. Ser.* **928** 012011 (2017)
213. Akhmetshin R R et al., in *Proc. of the Intern. Conf. on Instrumentation for Colliding Beam Physics, INSTR17, Novosibirsk, Russia*; *JINST* **12** C08010 (2017)
214. Anisenkov A V et al. *JINST* **12** P04011 (2017)
215. Druzhinin V P et al., in *Proc. of the 14th Intern. Workshop on Meson Production, Properties and Interaction* (*MESON 2016*): *Cracow, Poland, June 2 – 7, 2016*; *EPJ Web Conf.* **130** 05004 (2016); arXiv:1609.01040
216. Achasov M N et al. *Phys. Rev. D* **97** 012008 (2018); arXiv:1711.08862
217. Surin I K et al., in *Proc. of the Intern. Conf. on Instrumentation for Colliding Beam Physics* (*INSTR17*): *Novosibirsk, Russia*; *JINST* **12** C07043 (2017)
218. Achasov M N et al., in *Proc. of the 14th Intern. Workshop on Tau Lepton Physics* (*TAU 2016*): *Beijing, China, September 19 – 23, 2016*; *Nucl. Part. Phys. Proc.* **287 – 288** 57 (2017)
219. Achasov M N et al. *Phys. Rev. D* **94** 112001 (2016); arXiv:1610.00235
220. Achasov M N et al., in *Proc. of the 13th Pisa Meeting on Advanced Detectors*: *Frontier Detectors for Frontier Physics* (*FDFP 2015*): *La Biodola, Isola d'Elba, Italy, May 24 – 30, 2015*; *Nucl. Instrum. Meth. A* **824** 362 (2016)
221. Achasov M N et al. *Phys. Rev. D* **94** 092002 (2016); arXiv:1607.00371
222. Achasov M N et al. *Phys. Rev. D* **94** 032010 (2016); arXiv:1606.06481
223. Achasov M N et al. *JINST* **10** T06002 (2015)
224. Aulchenko V M et al. (SND) *Phys. Rev. D* **91** 052013 (2015); arXiv:1412.1971
225. Achasov M N et al. *Phys. Rev. D* **90** 112007 (2014); arXiv:1410.3188
226. Achasov M N, Kupich A S, in *Proc. of the Intern. Conf. on Instrumentation for Colliding Beam Physics* (*INSTR17*), *Novosibirsk, Russia; JINST* **12** C06035 (2017)
227. Korol A A, Melnikova N A, in *Proc. of the 17th Intern. Conf. on Calorimetry in Particle Physics* (*CALOR 2016*), *Daegu, Republic of Korea, May 15 – 20, 2016*; *J. Phys. Conf. Ser.* **928** 012010 (2017)
228. Carloni C M et al. *Phys. Lett. B* **746** 325 (2015); arXiv:1504.02228
229. Abbiendi G et al. *Eur. Phys. J. C* **77** 139 (2017); arXiv:1609.08987